

Scanning Tunneling Microscopy and Spectroscopy of Iron Pnictide Superconductors

Jochem Kaas

Master's thesis

Supervisor: Prof. dr. M.S. Golden

August 2010

Contents

1	Introduction	2
2	Experimental Methodology	5
2.1	STM theory	5
2.1.1	Set-up voltage effect	9
2.1.2	Direct LDOS pictures	10
2.2	STM practical matters	12
2.2.1	Approaching a sample	13
2.2.2	Tips	13
2.2.3	Cleaving of single crystal samples	17
2.2.4	Ultra-high vacuum	18
2.2.5	Temperature control	19
3	STM Applied to Pnictide Superconductors	22
3.1	Introduction to pnictide superconductors	22
3.2	Surface Morphology of the (122) and the (11) Pnictide Families .	26
3.2.1	BaFe ₂ As ₂	28
3.2.2	Fe _{1+y} Se _{1-x} Te _x	32
3.3	Spectroscopy	35
3.3.1	Spectroscopy of underdoped Ba(Fe _{1-x} Co _x) ₂ As ₂	36
3.3.2	Spectroscopy of Fe _{1.014} Se _{0.45} Te _{0.55}	40
4	Conclusion	43
	Acknowledgements	45
	Publication List	46
	Bibliography	47
A	Appendix: Beamtimes at BESSY	49

1 Introduction

Superconductivity is electrical conductivity with zero resistance. This phenomenon, first discovered by Heike Kamerlingh Onnes in 1911, has an interesting history, including some very recent developments. It also has an increasing amount of practical applications, for example in medical imaging technology, energy transport through power lines, and various scientific applications.

In 1911, Heike Kamerlingh Onnes was doing research into the electrical resistance of mercury at very low temperatures. He discovered that at temperatures below 4.2 Kelvin (4.2 degrees above absolute zero), mercury superconducts: it conducts electricity without any resistance. It is important to note that the resistance is not essentially zero or almost zero, it is truly exactly zero. Experiments were done with a superconducting ring, in which a current was made to run. If this ring were a normal conductor, the current would fully dissipate in a fraction of a second. The superconducting ring, however, kept its current for many years without a measurable decrease.

When the effect was discovered, there was no explanation for why superconducting materials behave the way they do. Kamerlingh Onnes expected the resistance of his mercury to approach zero closely as he reduced the temperature close to absolute zero. He certainly did not expect a sharp drop to zero at a non-zero temperature. In fact, when he first saw the effect, his first conclusion was that one of the wires in his measuring equipment must have shorted out. A theoretical explanation for the phenomenon of superconductivity did not arrive until 1957, when Bardeen, Cooper and Schrieffer proposed their theory of superconductivity, now called BCS theory.

In 1933, Walther Meissner discovered an additional property of superconductors now known as the Meissner effect: If a material is cooled to below its superconducting transition temperature while in a magnetic field, it will expel the magnetic field upon entering the superconducting state. The magnetic field lines, which were going through the material before the cooling, are forced to take a path around the material as soon as it becomes superconducting. This property does not follow directly from the fact that the electrical resistance is zero, it is an additional, separate effect. The Meissner effect is responsible for the fact that some superconductors can float above permanent magnets, or vice versa (see figure 1).

BCS theory predicts that the maximum temperature at which any material can superconduct is about 30 Kelvin. This made the discovery in 1986 of high-temperature superconductors especially surprising. Materials were found that superconduct at temperatures up to 135 Kelvin, over 4 times the limit proposed by Bardeen, Cooper and Schrieffer. High-temperature superconductors are not yet fully understood, and have been the subject of much research since their discovery. One thing that is certain is that BCS theory cannot fully explain how they work. Various pairing mechanisms other than the phonon interaction have been proposed, such as a magnetic interaction, but no consensus has been reached.

The high-temperature superconductors discovered in the 1980's are all com-

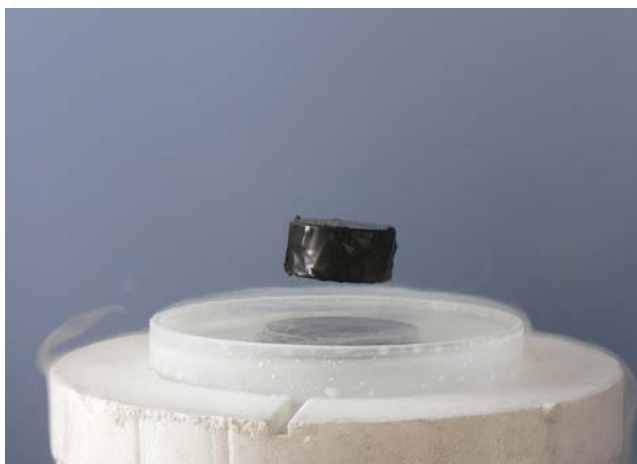


Figure 1: A magnet can levitate above a superconductor due to the Meissner effect. Photo by Mai-Linh Doan.

pounds containing the elements copper and oxygen, and they are collectively called the cuprates. Recently, in February 2008, a new class of superconducting compounds was discovered, the iron pnictides [1]. These are compounds containing the elements iron and arsenic. These compounds superconduct at temperatures up to 55 Kelvin. This is no competition for the cuprates, but their discovery has still initiated a rush of research. The hope is that research of the pnictides could lead to a greater understanding of both systems.

This thesis describes the study of these iron pnictides with scanning tunneling microscopy (STM). Section 2 will explain this powerful technique, which can be used for both atomic scale imaging and local spectroscopy. It is subdivided into first a theory section, explaining the operating principle of the STM and deriving some results essential to understanding scanning tunneling spectroscopy (STS). Second, there is a practical section, dealing with issues specific to the Createc LT-STM used in the experimental work reported here, as well as general issues, such as temperature control, preparation of tips, the cleaving of samples in ultra high vacuum (UHV), and the maintaining of this UHV.

Section 3 will introduce the pnictide superconductors more fully, delving into the atomic and electronic structure of the four families of pnictides. Then, the meat of the thesis: results. Topographic measurements will fully elucidate the surface structure of cleaved single crystals of two of the four families. Spectroscopic measurements are also presented, probing the electronic structure of the materials, with a focus on the superconducting gap.

Section 4 will concisely recap the conclusions drawn in this thesis and give an outlook to further STM studies of the pnictides.

The research in this thesis is part of ongoing research on the iron pnictide superconductors at the van der Waals-Zeeman Institute (WZI) at the University of

Amsterdam. A combination of resistivity measurements, STM, Angle-Resolved Photoemission Spectroscopy (ARPES), optical spectroscopy and Low-Energy Electron Diffraction (LEED) are performed in Amsterdam and at various synchrotron facilities. The goal of this research is to try to understand why the iron pnictides behave as they do. By probing the electronic structure of the iron pnictides with these techniques that give different, complementary information, we hope to be able to shed some light on the mechanism behind the superconductivity in these materials.

2 Experimental Methodology

2.1 STM theory

The basic principle of a Scanning Tunneling Microscope (STM) is that an atomically sharp metallic tip is brought to within a few Ångstrom of a surface to be studied. A voltage difference is applied between the tip and the surface, causing electrons to tunnel from the surface to the tip or vice versa. Classically, these electrons cannot enter the space between the sample surface and the tip, because they do not have enough energy, but quantum mechanical tunneling allows them to cross the gap with some nonzero probability. These tunneling electrons constitute a current flowing from the tip to the sample or vice versa, and the size of this tunneling current will depend on various parameters, one of them being the distance between the tip and the surface; if the tip is pushed closer to the surface, the current increases, and if it is pulled away, the current decreases. Typically, this height control is done by a piezoelectric material, which expands when a voltage is applied to it.

If the tunneling current is kept constant by controlling the height of the tip by varying the voltage applied to the piezo tube, the distance between the tip and the surface will remain constant. The tip can be scanned across the surface (i.e. moved in directions parallel to the surface), and, as long as the current is kept constant, will stay at a constant height above it, even if it is not completely flat. Any contours of the surface will thus be followed by the tip, see figure 2. The height of the tip required to maintain the set-point current can be calculated back from the voltage applied to the piezo tube, and so, a height map of the surface can be made. This is called a topographic image.

A topographic image is not the only thing that can be measured with the STM, however. To understand what else can be measured using this technique, it is instructive to look at the general expression for the tunneling current from the sample to the tip [2]:

$$I = \frac{2\pi e}{\hbar} \int_{-\text{inf}}^{\text{inf}} |M_{\mu\nu}|^2 g_{\text{sample}}(E) g_{\text{tip}}(E + eV_{\text{Bias}}) n_{FD}(E) [1 - n_{FD}(E + eV_{\text{Bias}})] dE \quad (1)$$

Here, $g_{\text{sample}}(E)$ and $g_{\text{tip}}(E)$ are the local density of states (i.e. the density of electron states of a certain energy, at the location of the tip) of the sample and the tip, respectively, while $n_{FD}(E)$ is simply the Fermi-Dirac distribution. This combination of densities of states and Fermi-Dirac filling fractions can be understood by realizing that an electron can only tunnel from a *filled* state in the sample ($g_{\text{sample}}(E) * n_{FD}(E)$) to an *empty* state in the tip of equal energy, taking into account the energy shift caused by the bias voltage ($g_{\text{tip}}(E + eV_{\text{Bias}}) [1 - n_{FD}(E + eV_{\text{Bias}})]$). See the right part of figure 2. This general expression was derived using only time-dependent perturbation theory (Fermi's golden rule), and hence, most of the real physics is still to be done: it is hidden in the matrix element $M_{\mu\nu}$ for a transition from state ψ_{μ} in the sample to state ψ_{ν} in the tip.

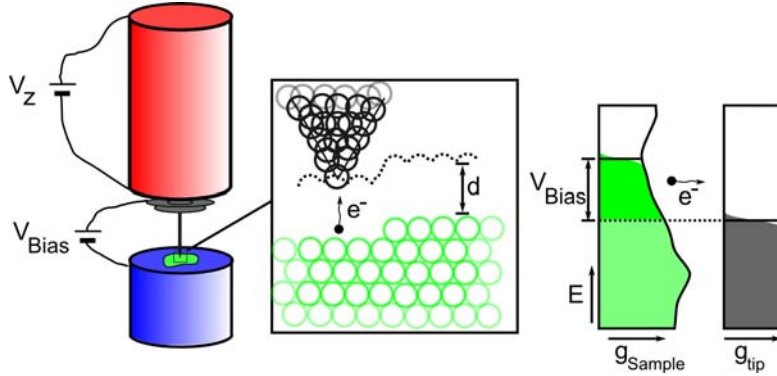


Figure 2: The operating principle of a Scanning Tunneling Microscope. On the left is the macroscopic view: The length of the piezo tube (red) depends on the voltage V_Z applied to it. This controls the distance between the tip (gray) and the sample (green), which is glued onto the sample holder (blue). The bias voltage V_{Bias} is applied to cause a nonzero tunneling current. In the center, the microscopic view: an electron tunnels across the vacuum gap between the tip and the sample. Keeping this tunneling current constant causes the tip to follow the contours of the surface (dotted line). Note: The typical tip-sample distance, about 5-10 Å, is shown to scale with respect to the real size of the atoms, which have a typical radius of 1-2 Å. The tip as depicted here is unrealistically sharp, however. On the right: The situation in energy/DOS space. The g_{Sample} and g_{tip} are the densities of states of the sample and tip. The bright green electrons can tunnel from the sample to the tip.

Before dealing with the matrix element itself, we can make two simplifying assumptions: firstly, we assume that $g_{tip}(E)$ does not depend on energy. This is a reasonable assumption for a metal tip, at least near the Fermi energy, but it can and should be checked for every tip (see section 2.2.2). Secondly, we take the zero-temperature limit: n_{FD} turns into a step function. With these assumptions, we can take $g_{tip}(E)$ out of the integral, and turn the Fermi-Dirac distributions into a change in the limits of integration. The current then simplifies to:

$$I = \frac{2\pi e}{\hbar} g_{tip} \int_{E_F}^{E_F + eV_{Bias}} |M_{\mu\nu}|^2 g_{Sample}(E) dE, \quad (2)$$

where E_F denotes the Fermi energy of the tip. Now, all that is left is to evaluate the matrix element $M_{\mu\nu}$. Bardeen shows in [3] that

$$M_{\mu\nu} = \frac{\hbar^2}{2m} \int d\vec{S} \cdot [\psi_\mu^* \vec{\nabla} \psi_\nu - \psi_\nu^* \vec{\nabla} \psi_\mu], \quad (3)$$

where the surface $d\vec{S}$ is any surface lying entirely in the vacuum between the tip and the sample. The integrand can be recognized as the probability current

operator; this expression is essentially just the probability current through a surface between tip and sample. To proceed further, a simplifying assumption must be made about the shape of the tip wavefunctions. We assume that the tip can be described, locally, by a sphere, at the place where it is closest to the sample. This assumption is made to make the overlap integral between the tip and surface wavefunctions manageable. The wavefunction for the surface can be kept general for a planar surface. For expressions for the wavefunctions, and a complete derivation of the matrix element, see [4]. The conclusion is that

$$M_{\mu\nu} \propto |\psi_{\mu}(\vec{r}_0)|^2, \quad (4)$$

where \vec{r}_0 is the center of the sphere that is modeling the tip. So this is simply the value of the wavefunction of the sample at a certain point above it. These wavefunctions drop off exponentially in the vacuum:

$$M_{\mu\nu} \propto |\psi_{\mu}(\vec{r}_0)|^2 \propto e^{-2\kappa d}, \quad (5)$$

where $\kappa = \frac{(2m\phi)^{\frac{1}{2}}}{\hbar}$, with ϕ the work function (the minimum energy difference between the Fermi level inside the material and a free electron state in the vacuum), and d is the height of the tip above the sample. We can return now to our expression for the current and find that

$$I \propto e^{-2\kappa d} \int_{E_F}^{E_F + eV_{Bias}} g_{Sample}(E) dE. \quad (6)$$

This exponential dependence of the current on the tip-sample separation is what makes STM such an accurate tool for measuring topographies. If $\phi = 4eV$, a typical value, $(2\kappa)^{-1} = 0.5\text{\AA}$, meaning the current changes by a factor e if the tip-sample separation is changed by a mere 0.5\AA . More interesting for fundamental physics, however, is the fact that the current is an energy integral of the density of states. If we take the derivative of the current with respect to the bias voltage, we get

$$\frac{dI}{dV_{Bias}} \propto g_{Sample}(E_F + eV_{Bias}). \quad (7)$$

Positioning the tip above the sample and then keeping it stationary while varying the bias voltage therefore gives us a direct probe of the local density of states of the sample, around the Fermi level. Since the current can go both ways, from the tip into the sample or vice versa, we can probe both the occupied and the unoccupied LDOS of the sample, unlike e.g. photoemission techniques, which can only probe the occupied states.

Earlier, we took the zero temperature limit. The effect of nonzero temperature will be a smearing out of the electron energies over a range of $k_B T$, or stated more formally: the measured LDOS at nonzero temperature will be the zero-temperature LDOS convoluted with the Fermi-Dirac distribution for that temperature.

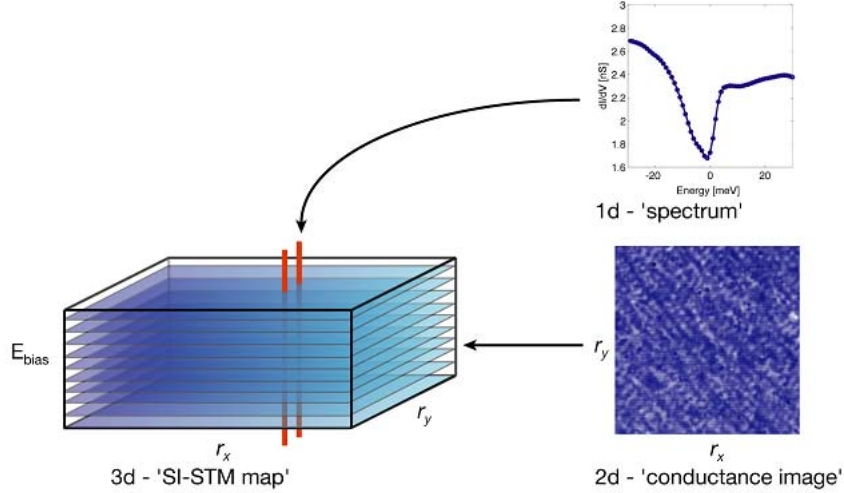


Figure 3: A full STS dataset with three dimensions: one energy dimension, and two spatial dimensions in the two directions of the sample surface. Two ways to “cut” through the dataset are shown: one gives a spectrum at a single point, and the other gives a two-dimensional picture of the LDOS at a certain energy. Adapted from [5].

This derivative of the current with respect to the bias voltage can be measured directly with a lock-in amplifier. The lock-in amplifier works by adding a small alternating voltage onto the bias voltage, with a known constant frequency. The current signal will then also alternate with this same frequency, with an amplitude that is proportional to $g_{Sample}(E_F + eV_{Bias})$. Using the alternating voltage that was applied as a frequency reference, it is possible to filter this current signal with a high accuracy, giving $g_{Sample}(E_F + eV_{Bias})$ as the output. This lock-in technique gives much better (i.e. less noisy) results than simply varying the bias voltage and taking the derivative numerically.

Choosing a location and sweeping the bias voltage across an energy region of interest, generally around E_F which is at zero bias voltage, gives us a spectrum $g(E)$ at that specific (x, y) location on the sample surface. If we take a grid of these spectra, i.e. a spectrum at every (x, y) location of a part of the sample surface, we get a three-dimensional dataset $g(E, x, y)$ with two spatial dimensions x and y and one energy dimension (see figure 3). If we now take a two-dimensional cut through this three-dimensional dataset, at a fixed energy E_0 , we have a picture of the variation of the local density of states as a function of position: $g(E_0, x, y)$. A picture like this, of the local density of states at energy E as a function of position, will henceforth be referred to as an (indirect) LDOS(E) picture. See section 2.1.2 for what we refer to as direct LDOS pictures.

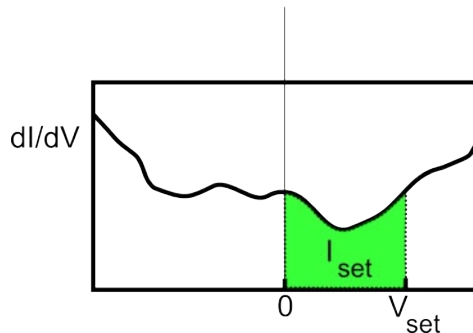


Figure 4: The set-up height effect. Every spectrum is normalized such that the shaded area, the integral of $\frac{dI}{dV_{Bias}}$ between $E = 0$ and $E = V_{Bias}$, is equal to I_{set} .

2.1.1 Set-up voltage effect

Above, it was stated that to obtain a spectrum, we position the tip above the sample and then keep it stationary while varying the bias voltage. However, it is relevant how high we position the tip above the sample. The height dependence is hidden in the proportionality constant in equation (7), but it is of course still present. The height at which a spectrum is taken is determined by the set-up current and voltage: the tip is positioned in such a way that it gives a certain current I_{set} with a certain voltage V_{set} . This is the only practical way to position the tip, but there is a problem with it: the resulting height depends on the local density of states, integrated from E_F to E_F plus the bias voltage. This is easily seen from equation (6). Effectively, every spectrum taken this way is normalized such that the area beneath it between $V_{Bias} = 0$ and $V_{Bias} = V_{set}$ is equal to I_{set} . See figure 4.

For single spectra, this normalization is not a problem: the absolute intensity of the spectrum simply does not contain any information, because its scaling is dependent on the set-up conditions. The relative intensities as a function of energy are what is relevant. For this reason, arbitrary units are used for the vertical axis of spectra in this thesis. The dimension of these arbitrary units is that of conductance, or Siemens (ampere per volt), the inverse of the Ohm. Their zero is well-defined, but their scale is arbitrary. On the horizontal axis will be the bias voltage, usually given in mV, so that 0 corresponds to the Fermi energy E_F .

When trying to draw conclusions from differences in intensities of spectra taken at different locations, as is done when making pictures of the local density of states as a function of position, care should be taken not to be confused by the set-up effect. Consider the hypothetical local density of states at two different positions as shown in figure 5. The two are identical except for a peak at small negative bias which is present in the red dashed spectrum and all but absent in the black one. If we take a positive V_{set} (left side of figure 5), the two

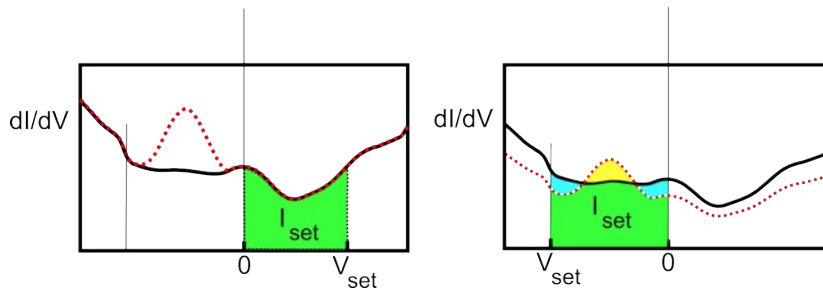


Figure 5: When comparing the values of spectra taken at different positions, the set-up voltage can be relevant. The relative values of the red and the black spectrum depend on the setup voltage. In this case, the two are equal at most energies when a positive setup voltage is used (left), but not when a negative setup voltage is used (right).

spectra coincide at all energies outside of the peak at small negative bias. If we then take an indirect LDOS(E) picture that involves these two locations at any energy E outside of the peak, there will be no difference in value between these two locations. However, if we use a negative V_{set} (right side), the tip will take a position at the red location that is further from the sample than at the black location, downscaling the red spectrum so that the shaded areas beneath both spectra will be the same. This causes the spectra to differ at all energies, even though the only difference in the actual density of states was at the peak just below E_F . An LDOS(E) picture will then also show contrast between locations with the peak and locations without the peak, even at energies outside the peak.

2.1.2 Direct LDOS pictures

The LDOS(E) picture that is created by cutting a grid of spectra at a certain energy was referred to as ‘indirect’. The direct way to make an LDOS picture is to simply scan across the sample as if taking a topographic image, while simultaneously recording the signal from the lock-in amplifier (with the modulation from the lock-in amplifier applied to the bias voltage). This gives the local density of states, not at an arbitrary energy as when making a cut through a grid of spectra, but only at the bias voltage used while scanning. This direct method has a few disadvantages compared to the indirect method:

- it cannot be used to determine LDOS(E) for very low energies. If the bias voltage is set to zero, the tip will be pushed into the sample (ruining it) because no current flows at zero bias no matter how close the tip is to the sample. For low but nonzero voltages, the risk of crashing the tip due to a small current fluctuation or vibration is high.
- In the indirect method, the set-up voltage and the energy at which the LDOS(E) is taken can be controlled separately. In the direct method, they

are necessarily the same. If the grid of spectra from the indirect method is cut at exactly the set-up voltage, the two methods will give the same result, but at other energies, the two methods may give different results due to the set-up effect described above.

- The direct method only gives a picture at a single energy at a time.

The great advantage of the direct method is speed. To get a sufficiently noise-free image, the scanning speed for direct LDOS data should be significantly reduced from the normal speed used to take topographic images, but it is still fast compared to the indirect method. For a rough idea: with the Createc LT-STM used to take the data in this thesis, a direct LDOS picture with 256x256 spatial pixels can be taken in about 45 minutes, while a full $g(E, x, y)$ dataset (e.g. 128x128 spectra from -25 to $+25$ mV) takes on the order of 12 hours to acquire. If the energy of interest is known beforehand and is not too low, and the energy dependence of the density of states is such that the set-up effect will not wash out the contrast between interesting features, the direct method should be more efficient than the indirect method.

2.2 STM practical matters

The picture in figure 6 shows the Createc low-temperature scanning tunneling microscopy (LT-STM) system that was used for all measurements in this thesis. Significant features that can be seen in the picture are:

- The black cylinders in the lower left. They are Newport I-2000 stabilizing legs, which protect the STM from vibrations coming through the floor, e.g. from a truck driving past the building. They work by floating the STM on a piston, which is supported by air pressure.
- On the far right and in the background, the two electronics racks, housing the control electronics for the STM.
- In the center, with all the windows: the main vacuum chamber, with a valve in the center separating the preparation chamber on the left side and the main STM chamber on the right side.
- Sticking out above the main vacuum chamber is the liquid nitrogen (outer) cryostat, which surrounds the liquid helium (inner) cryostat.
- In the foreground on the left, the transfer arm which allows us to manipulate samples and tips without breaking the UHV.
- Not visible here is the load lock; it is behind the main vacuum chamber in this picture. The load lock is used to insert samples and tips into the LT-STM without breaking the vacuum in the main chamber.

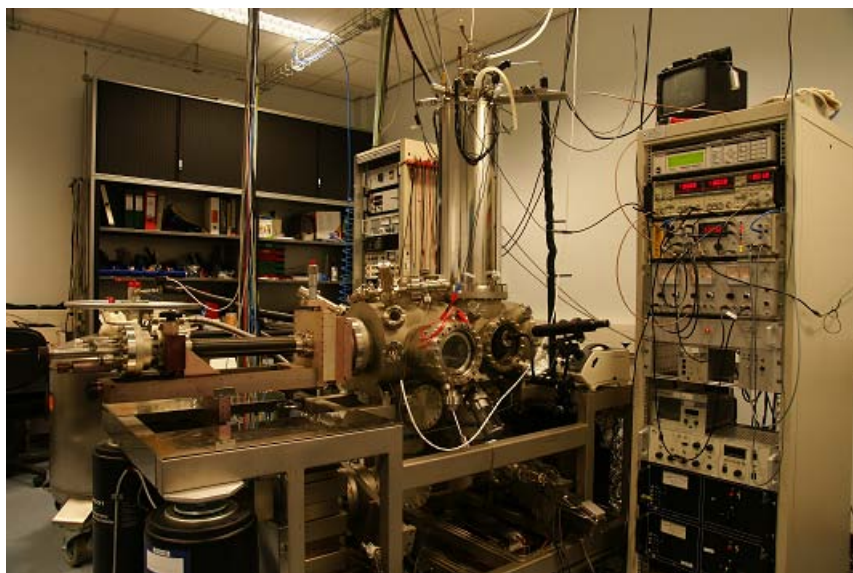


Figure 6: The Createc LT-STM system.

The STM block itself is only about the size of a human hand, and is suspended from the inner cryostat by springs, which further isolate the STM from outside vibrations. Vibrations are also damped by eddy current damping.

2.2.1 Approaching a sample

Once in the Createc LT-STM, a cleaved crystal, and the tip above it, can be seen from the side through a tiny window in the cryostat. This does not allow for easy depth-perception, so positioning the tip above the sample can be difficult. A good way to position the tip is by looking for the reflection of the tip in the sample. The point directly between the point of the tip and its reflection is where the tip would land if it were moved straight down. The Besocke-Beetle design has a tendency to move sideways while moving down, so it is best to move the tip as close as possible to the sample, without crashing into it, before starting the automatic approach.

The automatic approach works as follows: the tip is moved downward with the coarse approach mechanism by 1 step. Then, the z-piezo is extended until a tunneling current is detected. If a tunneling current is detected, the approach halts and the sample has been reached. If a tunneling current is not detected, the tip is still too high, and the coarse approach takes another step. This process continues until the sample is reached. The approach can take up to 30 minutes, depending on the height the approach was started at. If the approach takes longer than that, something is likely wrong. It occasionally happens that the approach does not halt at all. In this case, either the tip is too short to reach the sample and either the tip length or the sample height needs to be increased, or the tip has touched down on the sample but a tunneling current could not be established. This means that either the tip touched down on a non-conducting part of the sample, or the sample is not properly connected to the bias voltage. In both cases, the tip is ruined.

2.2.2 Tips

Tips in the Createc LT-STM are held by a tip-holder made of stainless steel, shown in figure 7. To transfer tips into and out of the STM, a “fork” is used, consisting of two prongs which fit in the groove of the tip holder. The tip holder is ferromagnetic, and held by magnets in the STM head. This allows it to stay firmly in place during measurements, but be easily removed simply by pulling it down, out of the magnetic field.

Tips were cut mechanically from 0.25 mm 80%Pt/20%Ir wire, with a required length precision of about 0.2 mm. This precision is required because the STM head coarse approach has a limited range. If the tip is too long, it will crash into the sample even if the coarse approach is in the fully retracted position, and if it is too short, it will not be able to reach the sample.

Cutting the tip was done with a simple pair of pliers. Surprisingly, this almost always results in an atomically sharp tip, or nearly so, with the right cutting technique. The best way is to put the pliers in a diagonal cutting



Figure 7: A tip. The tip itself is the thin wire sticking up from the center of the tip holder. The tip holder can be moved around in UHV by grabbing it with a fork that slides between the two discs of the tip holder.

position, then pull strongly on the wire while slowly increasing the pressure on the pliers until the wire is cut through. This way, when the wire is almost cut through and only a thin connection remains, the thin part of the wire can “flow” into a sharp tip because of the pulling force. Some attempts were made to improve the sharpness of these tips by etching, but for almost all the measurements presented, tips were inserted in the STM as cut. These proved to be sufficiently sharp to be usable, sometimes immediately, sometimes after a treatment with the help of the Au test sample.

Au test sample

The Au test sample is a gold crystal cut at an angle to reveal the (788) plane. This sample was used for calibration of the piezo tubes, and tip characterization and fixing. To maintain a clean and regular surface, it was sputtered and annealed periodically.

The (788) crystal plane [6] of Au, in the ideal case, consists of regularly spaced steps of 1 atom high and 16 atomic rows wide. The plateaus on top of the steps have the structure of the (111) plane, which the (788) plane is very close to in angle. Since the height of the steps is known (2.35 \AA), a topography image of this surface can be used to calibrate the z -piezo. A piezo tube responds to a voltage applied across it by expanding or contracting in length. The expansion or contraction is assumed to be proportional to the voltage. The proportionality constant of the z -piezo can be found with the Au sample, since it has known height variations. This was found to be 7.2 \AA/V for the new z -piezo installed in the LT-STM in October 2009.

Over time, because of the imperfect vacuum (typically on the order of $1 * 10^{-10}$ Torr), the Au sample can become contaminated with carbon or other materials.

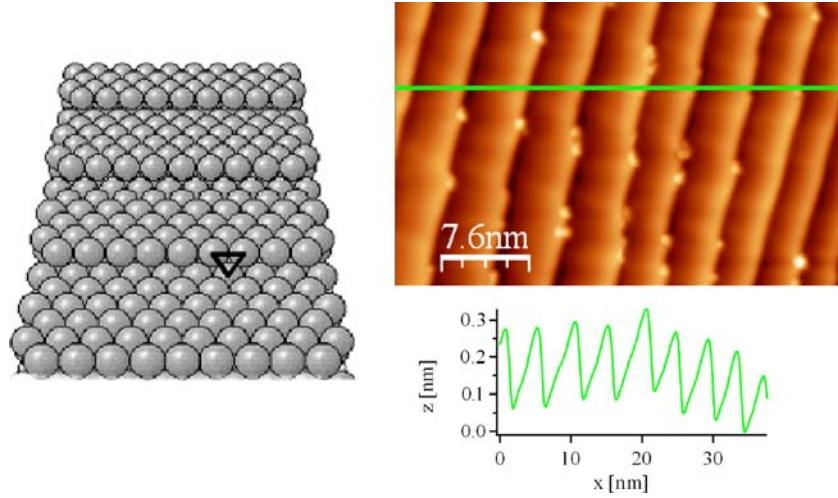


Figure 8: Left: Schematic picture of the steps in an Au vicinal surface. From [6]. Right: topographic image of our gold test sample. The linescan below it shows that the step edges are sharp, indicative of a sharp tip. This linescan is a “sawtooth” instead of a simple staircase because the Au(788) crystal direction is the vertical direction here, not the (111) direction which the terraces are perpendicular to. Note also the difference in horizontal and vertical scales in the linescan: the steps really are a single atom high and many atoms wide, as in the schematic picture on the left.

10^{-10} mbar) in the preparation chamber where the Au sample was kept, the Au surface acquired various adsorbed gases. These are visible as imperfections in the topography shown in figure 8. When these became too numerous, the adsorbed gases were cleaned off by sputtering with neon ions.

To sputter, a pressure of $1.5 - 2 \cdot 10^{-5}$ mbar neon gas was introduced into the preparation chamber. A sputtering gun then ionized the neon atoms and accelerated them onto the sample with a high voltage, 1.5 kV. The Au sample was grounded through a sensitive current meter, allowing us to measure the sputtering current of positively charged ions arriving on the sample. Sputtering at about $30 \mu\text{A}$ for 10 minutes gave good results.

After sputtering, the surface has been cleaned of the various adsorbed gases, but the ordered surface is also destroyed. To repair it, we annealed it for 1 minute at 700°C using the sample holder’s built-in button heater. This is not hot enough to melt gold, but it does give the surface atoms enough thermal energy to move around, so they can reorder into a well-ordered crystal.

Tip characterization

Every single tip is characterized on the Au test sample before use. Criteria for a good tip are: 1. Sharp topography images. 2. A constant $\frac{dI}{dV}$ as a function



Figure 9: Left: Sputtering the gold test sample. With the lab light completely dimmed and the vacuum gauge turned off, the ion beam is visible as a bluish glow. Right: Annealing the gold test sample. The required current causes the connecting copper wires to glow brightly.

of energy when measuring a spectrum on the Au surface, so that it satisfies the assumption that its density of states $g_{tip}(E)$ does not depend on energy. 3. Stable, not prone to spontaneous changes.

Figure 8 is an example of a sufficiently sharp image of Au (788). This does not show atomic resolution, but the terraces are so flat that only “strange” tips show atomic resolution on them. These strange tips are rarely stable for more than a minute of scanning, and never show a constant $\frac{dI}{dV}$. What causes these strange tips is not completely clear, but they are likely due to some impurity atom or molecule getting stuck to the end of the tip, with a non-spherical electron orbital sticking out.

As stated, a good tip should show a constant $\frac{dI}{dV}$ on Au, since Au is a simple metal, so its density of states is constant around E_F . For the measurements presented in this thesis, $g_{tip}(E)$ was checked up to $\pm 300mV$ on the Au test sample.

Sometimes, a tip turned out to be satisfactorily sharp and well-behaved as cut. Usually, however, it needed to be fixed: the few atoms or single atom at the very end of the tip that are responsible for the tunneling needed to be rearranged or replaced to improve the resolution and reliability of the images and spectra made by the tip. Fixing tips is more of an art than a science, but the recipe is as follows. To induce a change in the tip, have it scan over the Au surface with some ordinary tunneling parameters, e.g. $I = 40pA$, $V_{Bias} = 50mV$. Then, suddenly increase the voltage to $10V$, the maximum bias voltage the LT-STM electronics can deliver. This sudden change in voltage sometimes changes the tip, probably due to the high local electric fields that are present when the tip is still very close to the sample and the bias voltage is suddenly very high. Return to a sane bias voltage to check if the tip has changed, and repeat this process until the tip is good. If a tip is close to being good, be more gentle with it: use a lower current so that it’s further away from the sample, increase the voltage more slowly, go up to e.g. $7V$ instead of $10V$, et cetera. If a tip refuses to

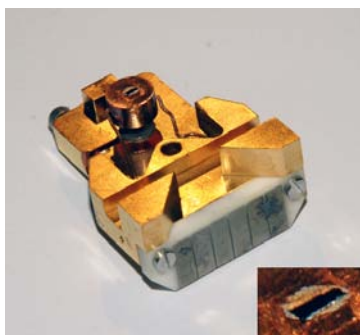


Figure 10: An example of a nicely cleaved pnictide crystal, on the sample holder used in the Createc LT-STM. The gray material surrounding the black shiny crystal is excess silver epoxy, which is used to glue the sample to the sample holder with an electrically conducting interface.

change, be more forceful with it. Another way to induce a change is to increase the setting of the integrator in the feedback loop. Increasing it sufficiently far will cause the feedback loop to resonate, which crashes the tip into the sample repeatedly.

2.2.3 Cleaving of single crystal samples

For surface-sensitive experimental techniques, including angle-resolved photoemission spectroscopy, low-energy electron diffraction, and, of course, STM/STS, a clean and flat surface is required. Fortunately, many interesting systems have a 2-dimensional (layered) structure, in which internally strongly bound layers of atoms are stacked on top of each other, with a weaker bond between the layers. This allows them to be readily *cleaved* for use in STM: with a small applied force, a monocrystalline sample breaks between these weakly bonded layers, exposing a single top layer.

A simple, well-known example of these layered structures is graphite, where the layers are covalently bonded internally, and held loosely together by van der Waals forces. Graphite has layers that are so weakly bound that it can be cleaved with a piece of scotch tape, by applying it to the (ab)-plane and removing it. Cuprate superconductors can also be cleaved this way, but the newly-discovered pnictides are slightly stronger. For the present research, samples were cleaved by gluing an aluminum post, with a wire loop on top of it, on top of the crystal, using Torr Seal UHV epoxy resin. The actual cleavage process was then performed inside the vacuum chamber, by sticking a tool through the wire loop and pushing sideways until the crystal breaks. By cleaving inside the vacuum chamber, we ensure that we have a fresh surface which has not been exposed to air. The Createc LT-STM setup that was used also has a facility to cleave at temperatures lower than room temperature, by cooling the end of the transfer arm on which the sample is held during the cleavage with liquid

nitrogen or liquid helium. This cryo-cleaving turned out to be relevant for the 122 family of pnictides (see section 3.2.1). After cleaving, the quality of the cleave was inspected optically. The criterion for a good cleave was a flat shiny surface sufficiently large to land the tip on.

2.2.4 Ultra-high vacuum

To keep samples clean during STM measurements at liquid helium temperatures, an ultra-high vacuum is required. Any gas molecules floating around will tend to stick to the extremely cold sample surface. These impurities can then stick to the tip when it passes over them, leading to unreliable results. So, considerable effort is expended on making sure the vacuum is as good as possible. Various pumping techniques are used.

The load lock, as the name implies, is used to insert new samples and tips into the UHV system. The load lock is vented, ideally with clean nitrogen gas, so that samples can be inserted by hand. Attached to the load lock is a turbo pump, essentially a very-high-speed fan. The fan blades rotate at $835Hz$, reaching pressures down to about $2 * 10^{-10}$ mbar in the load lock. The turbo pump requires a fore-vacuum in the order of 0.1 mbar to achieve these high speeds and low pressures. This fore-vacuum is generated by a scroll pump.

To reach pressures in the 10^{-10} mbar range in a reasonable amount of time, the load lock needs to be baked out. When exposed to air, the inside wall of the stainless steel vacuum chamber accumulates various gases, mainly water. If the vacuum chamber is simply pumped, these gases will be released very slowly, over a period of days/weeks, causing the pressure to decay very slowly to its final value. To greatly speed up this process, the load lock is heated from the inside by an infrared lamp, causing the stainless steel to release its gases much more quickly. Ideally, this is done overnight, but a few hours of baking can also give a satisfactory result when in a hurry.

When the pressure in the load lock is sufficiently low, the valve between the load lock and the preparation chamber can be opened, and the samples and tips transferred into the preparation chamber. Then, the load lock is closed again, and the pressure in the preparation chamber is allowed to recover (in tens of minutes) to the value it had before the load lock was opened. Then, finally, the samples and tip can be transferred into the STM head, which is in the main chamber. The preparation chamber and the main chamber are each pumped by a combination of an ion pump and a titanium sublimation pump. An ion pump works by ionizing gas molecules and atoms with a high voltage filament. These ions are then accelerated away from the filament by the same high voltage, and impinge on titanium electrodes, and are thus trapped. The (ion) current flowing between the filament and the electrodes, which are grounded, can be used to gauge the pressure in the chamber.

A titanium sublimation pump (TSP) is a titanium(-coated) filament, which can be heated by running a current through it, causing it to deposit a layer of titanium on the inside of the chamber it is in. Many gases readily undergo a chemical reaction with titanium (so called gettering), effectively removing them

from the vacuum. A subsequent heating of the filament will cover the reaction products with a fresh layer of titanium, burying them.

Ion pumps and TSPs work in a limited pressure range; they cannot be used to pump a system from atmospheric pressure down to ultra-high vacuum. Instead, they are used as a final stage, to reduce the pressure from a value reachable by the turbo pump on the load lock (10^{-9} - 10^{-10} mbar) to its final value (ideally, low 10^{-11} mbar). If the entire system needs to be vented for maintenance, the ion pumps are left off until the load lock turbo pump has evacuated the entire system. An oven can be built up around the system to bake it out. Baking the LT-STM for 4 days at 140 ° C turned out to be sufficient, after the system was vented in October 2009.

2.2.5 Temperature control

The Createc LT-STM head is kept cool by liquid helium in an inner cryostat, at a temperature of 4.2 K. The inner cryostat is inside the outer cryostat, which is filled with liquid nitrogen, at a temperature of 77 K. The cryostats are separated from each other by the chamber vacuum, with reflective shielding in between. This insulation and gradual transition from the room temperature exterior to the 4.2 K interior results in a low consumption of helium: A full tank of 4 liters of helium lasts roughly 3 days.

The maximum stand time, the longest time that measurements can be performed without interruption, is limited by the size of the liquid nitrogen vessel. It cannot be filled while the tip is in contact due to the vibrations filling causes. The new outer cryostat, installed in October 2009, has an additional thermal shield between the liquid nitrogen vessel and the room temperature exterior, reducing nitrogen boil-off. This should increase the maximum stand time from the previous value of 24 hours, though the new maximum has not been measured. This extra shield should also reduce any vibrations caused by the boiling nitrogen.

During operation, the STM head is suspended by springs from the inner cryostat. It is enclosed in a thermal shield which extends down from the inner cryostat. This puts the STM head, ideally, completely in a 4.2 K environment. The actual temperature during measurements is around 4.6 K. To adjust the sample temperature, a heater diode is used. This heater diode is mounted on the STM head. Because the thermal contact between the STM head and the cryostat (via conduction through the springs it is suspended from, and via radiation) is so weak, the heating power required is low, e.g. 4 mW to keep the STM head at 25 K.

In June 2009, a Neocera LTC-21 cryogenic temperature controller was installed. The LTC-21 is a PID-type controller, meaning its output power is a function of the difference ΔT between the measured temperature and the set-point (desired) temperature, with 3 terms: the Proportional term, which is proportional to ΔT with proportionality constant P , the Integral term, which is proportional to the time integral of ΔT over a time I before the current time, and the Derivative term, proportional to the time derivative of ΔT with propor-



Figure 11: The sample used for the temperature calibration. The wound wire leads to the thermometer diode, which is held in place by the small metal plate.

tionality constant D . The analog output of the LTC-21 was connected to the STM heater, and good PID values for this output were found to be $P = 100000$, $I = 9s$, $D = 2.25s$. These values were found via the Ziegler-Nichols PID tuning method [7]. They resulted in quick temperature steps, taking under a minute for temperatures below 15K, and high stability, with less than 1 mK variation over time.

The temperature sensor used to regulate the heater power and the sample itself are not in the same place on the STM head. Because of this, a possible concern is that when heating, the sample is not actually at the same temperature as the sensor. There could be temperature gradients in the STM head. The fact that the STM head (made of solid copper) should have a good internal thermal conductance compared to its heat contact with the 4.2 K environment should mean the temperature difference between the sample and the sensor will be low, but there might still be a discrepancy.

To measure this discrepancy, if any, an experiment was performed where a separate temperature sensor was placed where the sample to be studied normally is (see figure 11 and compare with figure 10). With this thermometer in place, the heater was set to make a step in temperature, and the temperature response at the location of the sample was measured. An example of a temperature step, this one from 20 K to 25 K, is shown in figure 12. After the STM reached its set temperature, in this case after 10 minutes, the temperature at the sample was observed to rise with a decaying exponential to a final value, as should be expected. For this temperature step, the final value was 24.4 K, giving a difference between the sample temperature and the set-point temperature of 0.6 K. This difference, as a function of the set-point temperature, is plotted in figure 13. Reassuringly, the temperature difference was less than 1 K at temperatures lower than 25 K.

The decay time of the sample temperature (8.94 minutes for the step in

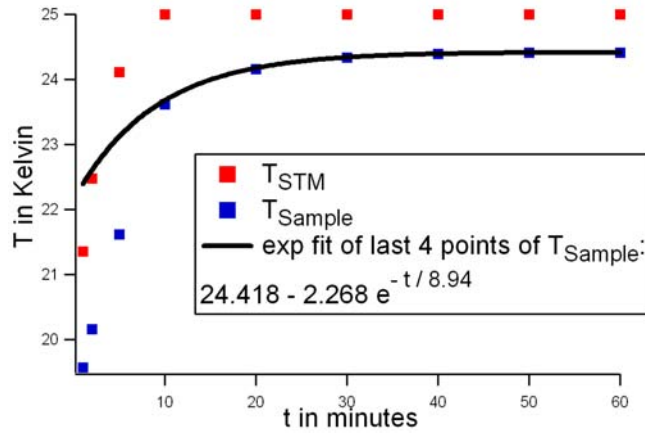


Figure 12: A step in temperature. The red data points are the temperature of the STM block as measured by the thermometer that controls the heater. The blue data points are the actual temperature at the sample as measured by the calibration thermometer.

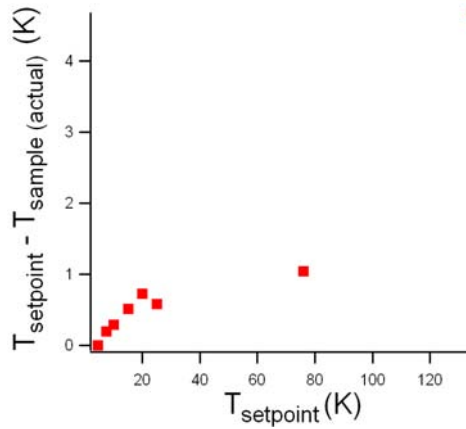


Figure 13: The result of the temperature calibration. The temperature at the sample is slightly lower than the temperature of the STM block at all temperatures, but not by more than 1 K in the relevant temperature range.

figure 12) is also a relevant result: After a large temperature step, it takes at least half an hour for the actual sample temperature to reach its final value, even if the sensor on the STM has already reached its set-point temperature.

3 STM Applied to Pnictide Superconductors

3.1 Introduction to pnictide superconductors

The iron pnictide family of superconductors broadly consists of four subfamilies, shown in fig. 14 (a)-(d). The structural unit that is common to all the families, the place where the interesting physics happens, is the FeAs layer, shown in fig. 14 (e). The iron (Fe) atoms in the FeAs layer are arranged in a square lattice with a lattice constant of roughly $a_{Fe-Fe} = 2.8\text{\AA}$. The arsenic (As) atoms surround the Fe atoms in their tetrahedral positions, resulting in As layers on either side of the Fe layer, each consisting of a square lattice of As atoms with a lattice constant of $a_{As-As} = \sqrt{2}a_{Fe-Fe} = 3.9\text{\AA}$.

The first three families differ in what separates the FeAs layers. The (1111) family, despite displaying the highest superconducting transition temperatures (up to $56K$), is rarely studied, as is the (111) family. The reason for this is that for these compounds, it seems to be much more difficult to grow sufficiently large single crystals, which are essential for many experimental techniques, including STM. This leaves the (122) family, which is considered by many to be representative of the pnictides as a whole, and the (11) family, which is an odd one out. The (11) family, rather than consisting of FeAs layers, consists of e.g. FeSe layers, without any separating layers. It is therefore not quite right to call it a pnictide, literally meaning a compound containing an element from the nitrogen group of the periodic table (including phosphorus, arsenic, antimony); rather it is more correctly called a chalcogenide, after the group of elements including selenium and tellurium.

The four families all display broadly similar physics. It seems to be that the FeAs layer is where all the interesting physics is going on: the Fe 3d electrons are responsible for the low lying electronic structure [8].

the conduction electrons are the Fe 3d electrons [8].

To illustrate the variety of interesting physics going on in the pnictides, we can look at the phase diagram (figure 15). This shows the properties of the system, specifically BaFe_2As_2 , as a function of temperature (vertical axis) and cobalt (Co) doping (horizontal axis). The parent compound, i.e. BaFe_2As_2 without any doping, crosses over from the normal state at high temperatures into an antiferromagnetic spin-density wave (SDW) state around $135K$. In this state, the electron spins localized on the Fe atoms are aligned in the same direction along the b axis, and in alternating directions along the a axis (see arrows in fig. 14(e)). This magnetic transition goes hand in hand with a structural transition from the tetragonal state, in which the a and b directions are identical, to the orthorhombic state, in which the a axis lattice parameter becomes up to about 1% larger [10] than the b axis one.

The parent compound BaFe_2As_2 can be doped in various ways. One possibility is to replace some Fe atoms by Co atoms, giving a composition of $\text{Ba}(\text{Fe}_{1-x}\text{Co}_x)_2\text{As}_2$. Upon doping with cobalt, the structural and SDW transitions start being suppressed, the SDW transition slightly faster than the structural one. At $x \approx 0.03$, superconductivity sets in. For cobalt doping

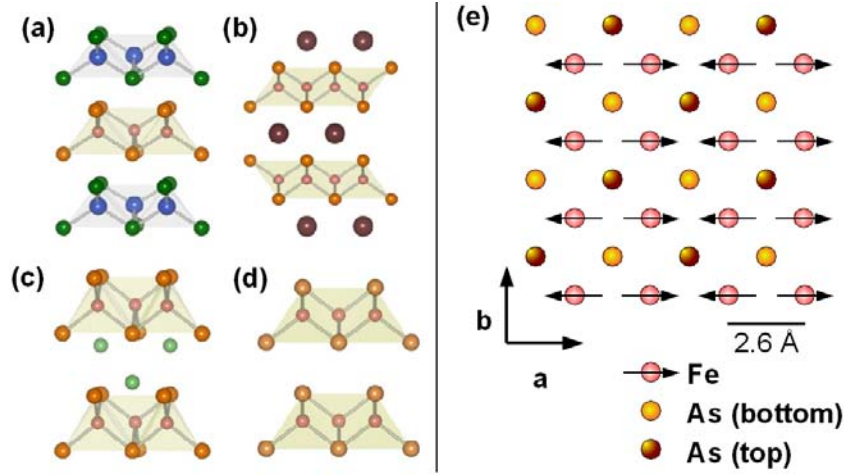


Figure 14: The 4 pnictide families. (a) The (1111) family. The FeAs layers are separated by e.g. LaO layers, which are structurally similar to the FeAs layer. This gives a composition of LaFeAsO (1111). Other compounds in this family include NdFeAsO , SmFeAsO , CeFeAsO . (b) The (122) family. The FeAs layers are separated by single layers of e.g. barium, giving a composition of BaFe_2As_2 (122). Other compounds in this family include EuFe_2As_2 , CaFe_2As_2 . (c) The (111) family. The FeAs layers are separated by double layers of e.g. lithium, giving a composition of LiFeAs (111). Another compound in this family is NaFeAs . (d) The (11) family. The simplest structure, it is actually composed of FeSe layers rather than FeAs, with no separating layers. Tellurium can be substituted for the selenium in any amount, giving a composition of $\text{FeSe}_x\text{Te}_{1-x}$, x ranging from 0 to 1. (e) A single FeAs block, top view (along the c axis). Arrows on the Fe atoms indicate the spin-density wave order. (a)-(d) adapted from [9]

of BaFe_2As_2 , the maximum T_c is 24 K, around $x = 0.07$ (optimum doping).

The replacement of Fe by Co should constitute electron doping: Co has an extra 3d electron compared to Fe. One could wonder if this electron doping is essential to the disappearance of the SDW and the appearance of superconductivity. This turns out not to be so: replacing barium by potassium (K), nominally hole doping, also induces superconductivity, up to 38K for $\text{Ba}_{0.6}\text{K}_{0.4}\text{Fe}_2\text{As}_2$ [12]. Even an isovalent substitution such as phosphorus instead of some of the arsenic atoms has the same effect, with $T_c = 30\text{K}$ in $\text{BaFe}_2(\text{As}_{0.68}\text{P}_{0.32})_2$ [13]. This is thought to be due to the chemical pressure that the (smaller) P atoms cause. Applying (regular) pressure to the parent compound also has similar effects, with superconductivity up to 29K at a pressure of 4GPa [14]. Plotting the phase diagram of BaFe_2As_2 as a function of hole doping ($\text{Ba} \rightarrow \text{K}$), chemical pressure ($\text{As} \rightarrow \text{P}$), or regular pressure gives the same overall shape as for electron doping: The structural and SDW transitions are suppressed, and when

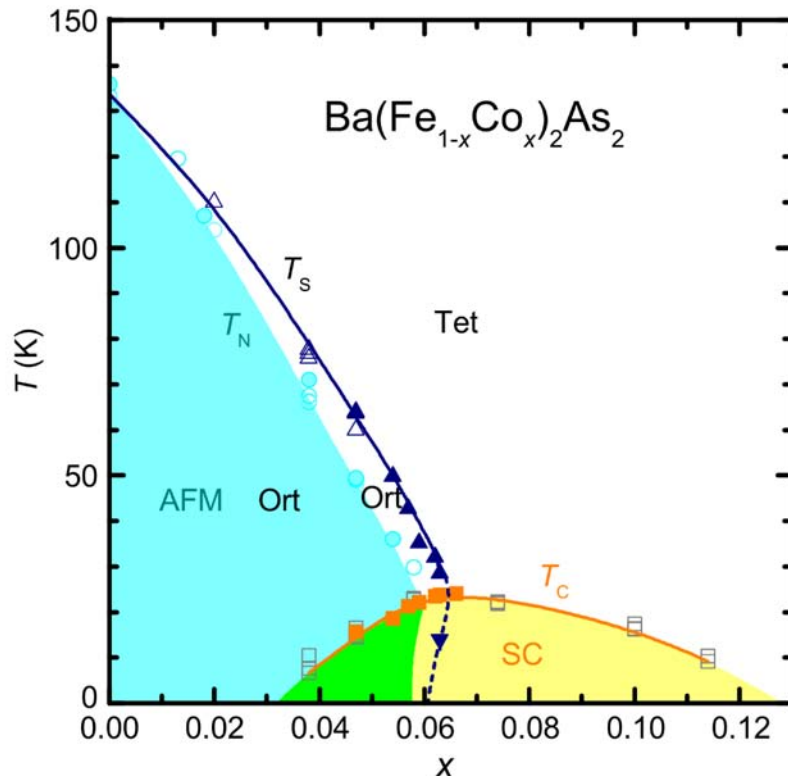


Figure 15: The phase diagram of $\text{Ba}(\text{Fe}_{1-x}\text{Co}_x)_2\text{As}_2$ as a function of temperature and cobalt doping. A structural transition (at T_S) from tetragonal to orthorhombic and a magnetic transition (at T_N) to a spin density wave (SDW) state go roughly hand in hand. A superconducting dome (SC) appears with cobalt doping. Adapted from [11].

they are (almost) gone, a superconducting dome appears.

There are a few current theories for the mechanism behind superconductivity in the pnictides. It was realized very early, even before pnictides with a T_c above the BCS limit were found, that phonons could not be responsible for the pairing interaction [15]. The electron-phonon interaction is simply not strong enough.

One attempt to explain the physics in the pnictides was made using the concept of *electronic polarons* [16]. The iron atoms in the pnictides are surrounded by 4 arsenic atoms, which can be seen as huge (relatively speaking) polarizable electron clouds. An extra electron on an iron lattice site will polarize these clouds, leading to a charge configuration like the one in figure 16a. This combination of an electron and the distortions in the electron cloud of the surrounding As atoms is called an electronic polaron.

Working out the Hamiltonian for these polarons, it turns out that they

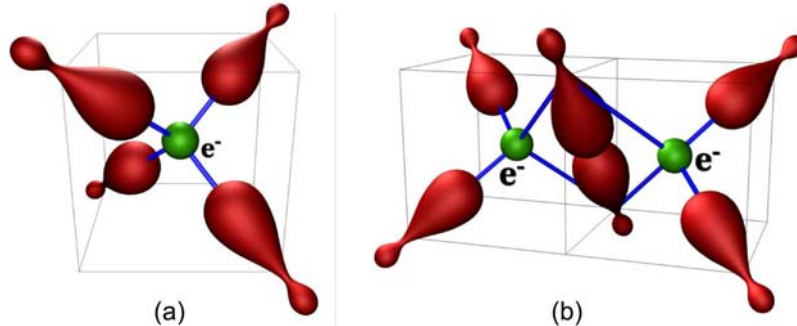


Figure 16: (a) A single electronic polaron, consisting of an electron on an iron site and the polarization of the 4 arsenic atoms surrounding it. (b) A bipolaron, a bound state of 2 polarons. Shown here is the case that the electrons are on nearest-neighbor sites. From [16].

interact with each other attractively, leading to bound pairs called *bipolarons* (fig 16b). These bipolarons can be nearest-neighbor (as shown in the figure) or on-site, with the electrons on the same iron site. Second-nearest neighbor bipolarons are unstable to dissociation into two single polarons. The existence of on-site bipolarons is mentioned [16] as a (partial) reason why the pnictides are only moderately correlated: the Hubbard U , the repulsion between two electrons on the same site, is roughly equal to W_{Fe3d} , the bandwidth of the conduction band [17][18]. Bipolarons are thought by some to be relevant to the superconductivity as well; they could have a role similar to Cooper pairs in conventional superconductors.

Another key concept in understanding the pnictides, currently the most supported by experimental results as being responsible for the superconductivity, are spin fluctuations. The superconducting dome of the pnictides is near (in the 1111 family) or overlapping (in the 122 family) an SDW state. Superconductivity only appears when this SDW state is (almost) destroyed by doping or pressure, but of course, the critical fluctuations associated with this state are still present. These spin fluctuations could be the pairing mechanism in the pnictides, with theory predicting T_c s up to $60 - 80K$ [19], consistent with the maximum known T_c of $56K$.

Spin fluctuations, which are also thought to be responsible for the unconventional superconductivity in the cuprates and the heavy-fermion materials, can only induce a superconducting order parameter with a triplet character, or one with a singlet character that changes its sign over the Fermi surface. For the heavy fermion materials, this is a p -wave (triplet) order parameter, while for the cuprates it seems to be a singlet d -wave. In the pnictides, most evidence points [10] to a so-called $s\pm$ [15] state, which is isotropic but has a 180° phase shift between different parts of the Fermi surface.

3.2 Surface Morphology of the (122) and the (11) Pnictide Families

*The contents of this subsection were published in part as “Cleavage surfaces of the $BaFe_{2-x}Co_xAs_2$ and $Fe_ySe_{1-x}Te_x$ superconductors: A combined STM plus LEED study”, F. Masee, S. de Jong, Y. Huang, J. Kaas, E. van Heumen, J. B. Goedkoop, and M. S. Golden, *Phys. Rev. B* 80, 140507(R) (2009).[24]*

There are many techniques for studying the properties of matter in its solid state. Some of them, notably angle-resolved photoemission spectroscopy and STM itself, are surface sensitive. This means that they only probe the electrons in the top few atomic layers of a material. To properly interpret the results of these techniques, it is important to know the surface structure of the material to be studied. In the case of layered materials like the pnictides, the two major questions to be answered are: which atomic layer is exposed upon cleaving the material? And are there significant deviations from the bulk atomic structure at the surface, and if so, do they impact the surface electronic structure?

The first question can be considered theoretically. The pnictides are composed of a number of elements, each of which has a different tendency to attract electrons. Arsenic atoms, for example, are “happiest” when they have 3 extra electrons, putting them in a noble gas configuration. These electrons come from the other atoms in the compound, leaving them positively charged. The end result, in the case of the pnictides, is that they consist of layers of charged atoms. These layers, viewed from sufficiently far away to not be affected by their microscopic structure, can be considered to be a plane with a certain charge per unit area, e.g. $\rho = -3e/a_{As-As}^2$ for an arsenic plane.

An infinite charged plane has a nonzero electric field that is constant in magnitude over all space, pointing away from the plane, and thus has an electrostatic potential which grows linearly with the distance from the plane (this can be easily concluded from the theory of electrostatics). This gives a diverging contribution to the electrostatic energy of an ion in the solid far away from the charged plane; an unphysical situation. The resolution lies, of course, in cancellations of the terms from differently charged planes. However, this requirement for cancellation does restrict the cleavage possibilities of a layered crystal.

To better understand this, we must define some terminology, proposed by P.W. Tasker [20]. He distinguished 3 types of stacking sequences of charged planes. Type 1 has planes that contain equal amounts of positive and negative charge, resulting in neutral planes overall. Type 2 (see figure 17a) does have charged planes, but they are stacked in such a way that the structural repeat unit does not have a net dipole moment perpendicular to the planes. Type 3 (figure 17b) also has charged planes, but stacked in such a way as to have a nonzero dipole moment in each structural repeat unit. It is this third type which cannot possess a low-energy, unreconstructed surface in nature. The simplest example of a structural repeat unit with a dipole moment is a layer with a single positive charge per atom on top of a layer with a single negative charge per atom.

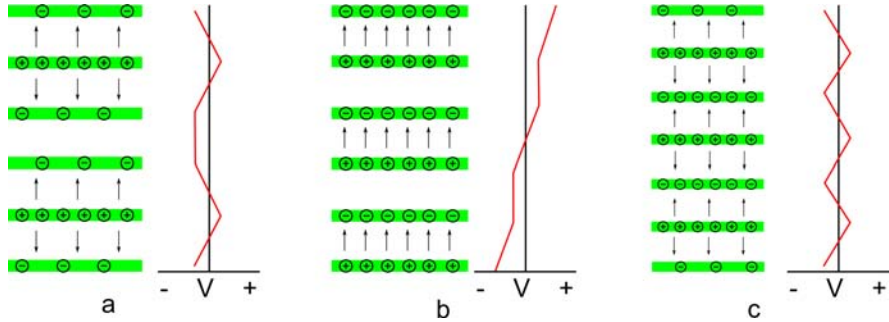


Figure 17: (a) An example of a structure of charged planes with a zero dipole moment in the structural repeat unit (type 2). The negatively charged layers have half the charge density of the positively charged layers. Shown alongside is the electric potential this crystal would have: it is well-behaved. (b) An example of a structure of charged planes with a nonzero dipole moment in the structural repeat unit (type 3). Its electric potential grows linearly with the number of layers, leading to a divergence when the crystal is arbitrarily large, as crystals can be. (c) The same structure as in (b), but with half a layer of charge moved from the top of the crystal to the bottom. This removes the net dipole by changing the structural repeat unit. Its potential is again well-behaved.

These dipoles, having a net charge of zero, do not have a nonzero electric field at large distances, and thus also no divergent electrostatic potential at large distances. They do, however, have a nonzero potential that is constant in magnitude, positive on one side of the dipole and negative on the other. Or, phrased differently, because the zero point of the potential is arbitrary: the potential is constant outside of the dipole, but with a different value on one side than on the other. In a crystal where many of these dipoles are stacked, this again gives a divergent contribution to the electrostatic energy of every ion. This is called the polar catastrophe, and is the reason this type of crystal surface does not exist without significant reconstruction.

Up to now, this issue has been presented as being a result of different stacking orders of charged planes. However, the true problem lies in the surface. Compare, for example, the model crystal in figure 17b with the one in 17c. In the “bulk”, they have the same structure, but they have a different termination surface: essentially, to transform 17b into 17c, we have to move half a layer of negative charge from the top of the crystal to the bottom. The result is a crystal in which the potential is well-behaved.

We can conclude that we can have a good idea in what plane layered crystals will be likely to cleave, as long as we know the charge distribution in them. Some cleavage planes will result in a polar surface, which must be reconstructed in some way, which is energetically unfavorable, while other cleavage planes result in non-polar surfaces. What all this implies for the cleavage surface of the (122) and (11) families of the pnictides will be explored in the following sections.

3.2.1 BaFe₂As₂

The (122) family displays a wide variety of topographies in STM. A selection from the “zoo” is displayed in figure 18. In 18a, we see one-dimensional stripe features with a spacing of $2a_{As-As}$ or about 8 Å. In 18b, we see a square lattice with lattice constant $a_{\sqrt{2}} = \sqrt{2}a_{As-As} = 5.6\text{Å}$. Figure 18c shows these two surface types in the same field of view, showing that one can transition into the other, without a significant change in height that would indicate that they represent different layers of the crystal. The smooth, relatively structureless part on the right is the $\sqrt{2}$ lattice shown in a, as it is usually imaged; figure a was made with an unusually sharp tip. Figure 18d shows a disordered maze-like surface. It is not completely random; two directions, at 90° angle to each other, dominate the picture. Figure 18e shows a disordered surface, with some similarities to 18d, but here, single atoms can be distinguished in some places. The right part of figure 18f shows what we have come to call ‘rods’: 1.5 Å high features, here parallel to stripes similar to those in 18a. A natural question to ask is: what could possibly give rise to this multitude of qualitatively different surfaces? In this section, it will be argued that it is a half-layer of barium atoms, which can be arranged in various ways to result in a variety of topographies.

There has actually been some controversy about the cleavage surface of the (122) family. For example, Nascimento et al. [21] conclude from a combination of STM and LEED measurements that the layer that is exposed upon cleavage is the arsenic layer. In [21], they present images of a square lattice with lattice constant 5.6Å, similar to figure 18b. They attribute this to the orthorhombic structure, which contains two symmetrically distinct arsenic atoms per unit cell: for one, the 4 underlying iron atoms are slightly closer than they would be in the tetragonal structure, and for the other, they are slightly further away. Apparently, they conclude, one of these two is more visible in STM than the other, leading to this square lattice showing half of the present arsenic atoms.

In [22], the same group presents images of a stripe pattern similar to figure 18a. They attribute these features to a dimerization of arsenic atoms: rows of arsenic atoms, spaced 4 Å apart in the bulk, move together in pairs at the surface, resulting in dimerized rows that are 8 Å apart. The group also presents LEED I(V) measurements. They compare these to theoretical curves for three possible scenarios: cleavage with an arsenic layer as the top layer, with a full barium layer as the top layer, and with iron as the top layer. They conclude that an arsenic layer as the top layer gives the best match.

What is not mentioned by Nascimento et al. is that all three of the suggested terminations would result in the creation of a polar surface. At first glance, the (122) family is a type 3 crystal, using the nomenclature of the preceding section. The layers have the following charges, in the order they are present in the crystal: the barium layer has a charge of +2, the arsenic layer has a charge of -3, the iron layer has a charge of +4 (the iron atoms have a +2 charge each, but the layer is twice as numerically dense as the other layers), and the next arsenic layer also has a charge -3. If the crystal cleaves between the barium layer and the arsenic layer, with the arsenic layer being exposed as the top layer, then

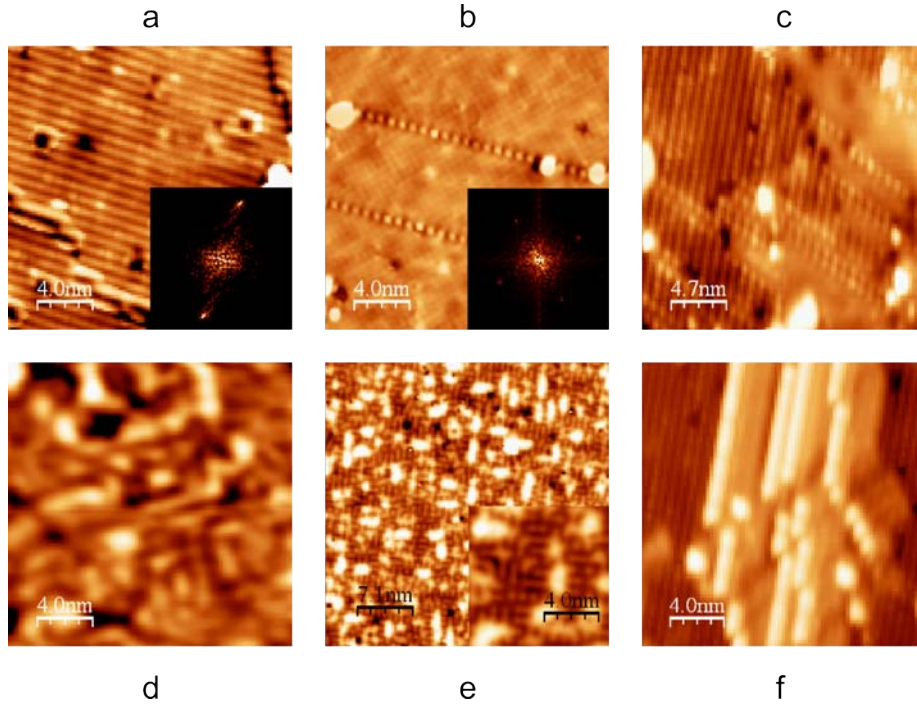


Figure 18: Various topographies seen on the BaFe_2As_2 surface. (a) 2×1 reconstruction, (b) $\sqrt{2} \times \sqrt{2}$ reconstruction, (c) 2×1 and $\sqrt{2} \times \sqrt{2}$ in the same field of view, (d) “maze-like”, (e) disordered with visible atoms, (f) ‘rods’.

the structural repeat unit has charges $(-3, +4, -3, +2)$. This structural repeat unit has a dipole moment. The other two scenarios considered by Nascimento et al. are no better: barium as the top layer gives us charges of $(+2, -3, +4, -3)$, with a dipole moment just as large as in the arsenic case but in the opposite direction. Iron as the top layer is even worse, with charges $(+4, -3, +2, -3)$: a dipole moment twice as large as the previous two cases.

A polar surface seems to be unavoidable. However, there is a resolution: a cleavage that leaves half of a barium layer on either side of the cleave. A plane with half the number of barium atoms that is present in the bulk effectively has a charge of $+1$, instead of $+2$. This gives a structural repeat unit with charges $(+1, -3, +4, -3, +1)$, which is symmetric and thus has no dipole moment. Here, we have mentally split each barium layer in the bulk into two half-layers, one part of the structural repeat unit above it, and one part of the unit below it. A similarly symmetric cleavage plane would split the iron layer in half instead of the barium one, but this cleavage scenario is highly unlikely due to the fact that the entire FeAs block is covalently bonded, making it energetically strongly unfavorable to break it apart. So, we hypothesize that the cleavage leaves half of a barium layer on either side of the cleavage plane.

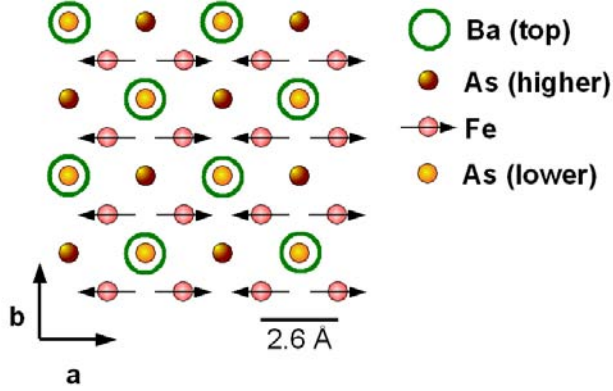


Figure 19: The structure of the (122) family, seen along the c -axis.

Figure 19 shows a top view of the structure of 4 layers of a (122) crystal: A full barium layer and the underlying Fe-As block. The full barium layer is a square lattice with lattice constant $a_{Ba-Ba} = 3.9\text{\AA}$. The hypothesis is that the top layer of the cleaved crystal is half of this barium layer. The remaining half layer could be arranged in various ways, some examples of which are shown in figure 20. We assume here that the barium atoms are still in their bulk positions, but that half of them are missing. Two possibilities for an ordered way to arrange the half layer are the so-called 2x1 reconstruction, shown in 20a, and the $\sqrt{2} \times \sqrt{2}$ reconstruction, shown in 20b. In the 2x1 reconstruction, alternate rows of atoms are removed. This results in rows of atoms that are spaced $2a_{Ba-Ba} = 8\text{\AA}$ apart, lying in one of the directions of the original barium lattice. The $\sqrt{2} \times \sqrt{2}$ reconstruction is again a square lattice, but with a lattice constant that is $\sqrt{2}$ times higher (5.6\AA), and rotated by 45° with respect to the original square lattice: this is the same direction as the iron lattice. Another possibility is large conglomerations of barium atoms that are in the bulk configuration, as in figure 20h. These could result from a local excess of barium atoms, or would otherwise have to be paired with areas where the arsenic layer is locally exposed. Finally, we could imagine a disordered half-layer, where atoms are randomly scattered across the possible sites, e.g. figure 20d. Figures 20e-g show some possibilities for deviations from long-range order in the two ordered surface types (a and b), and 20c is a transition between the two.

If the surface of our BaFe_2As_2 crystals is indeed a barium half-layer, this model should account for all the variation we see in the STM topographs; of course, it does. The striped structure with 8\AA spacing shown in figure 18a is the 2x1 reconstruction of figure 20a. The individual atoms in the lines are never resolved with normal tunneling parameters, but with a sufficiently low tunneling resistance they can be seen [23]. The 5.6\AA square lattice shown in figure 18b is the $\sqrt{2} \times \sqrt{2}$ reconstruction of figure 20b, with the “ladders” that run at 45° to the lattice directions representing a shift of part of the lattice by one atom, as shown in 20f. These ladders could equivalently be considered to be tiny areas of

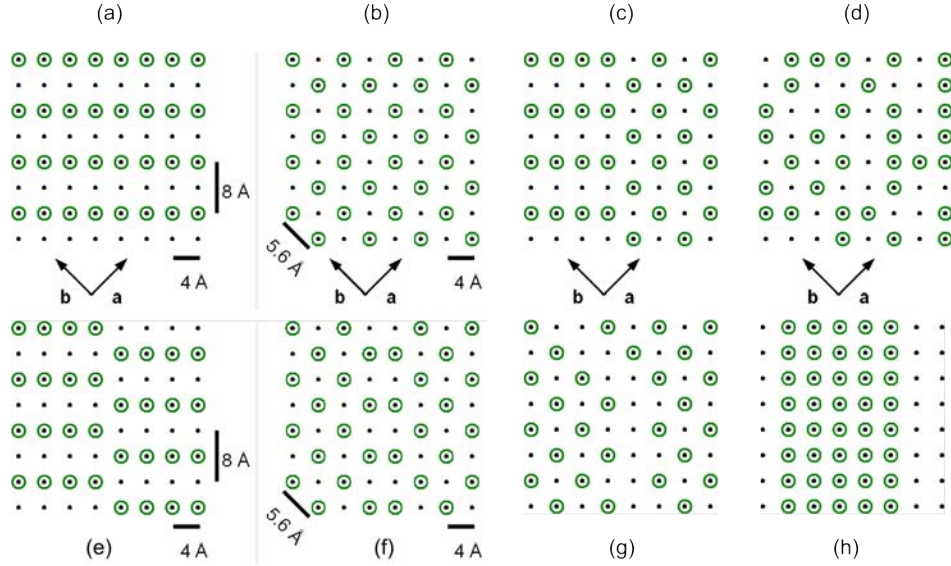


Figure 20: Examples of different arrangement possibilities for the half-layer of barium. A black dots are the lattice positions as they would be for a barium layer in the bulk. The green circles are barium atoms actually occupying a position: for a half-layer of barium, half of the possible positions would be filled.

the 2×1 reconstruction included in the $\sqrt{2} \times \sqrt{2}$ lattice. Figure 18c shows larger inclusions of the 2×1 structure in the $\sqrt{2} \times \sqrt{2}$ (here not atomically resolved), and a transition between the two as illustrated by figure 20c. Also visible in the left part of the image is an example of a shift in the 2×1 reconstruction, like in 20e.

Figures 18d and 18e are examples of the disordered barium half-layer shown in 20d. Looking at the inset of 18e, it seems like, in places where the barium atoms are close together, their electrons join together to form large featureless clouds, while atoms that are not surrounded by neighboring atoms can be resolved as single balls. The fact that there are no resolved atoms in 18d is probably simply due to sub-optimal tunneling conditions, probably a poor tip.

From all this, we can state with confidence that the surface we see in STM is a half-layer of barium. This conclusion should be transferable to any other compound in the (122) family, although calculations show that the relative energy of the different reconstructions is dependent on the specific compound: e.g. for BaFe_2As_2 , the $\sqrt{2} \times \sqrt{2}$ reconstruction is energetically favored over the 2×1 (though we do see both), while for CaFe_2As_2 the 2×1 is favored [25].

It seems plausible that these barium atoms on the surface might have a tendency to move around. It's only a small jump for a barium atom to move from the lattice site it is occupying to an empty one, which might be equally or even more favorable energetically. We might expect to see the STM topography

change occasionally, with the rate of changes depending on the temperature. However, at the temperatures in our STM, we have not seen these spontaneous movements at all, even over weeks of measurements on the same piece of surface at $4.2K$, and days at temperatures up to $27K$ during temperature dependent spectroscopy measurements. At higher temperatures, around $200K$, the surface does “melt”; this can be concluded from LEED investigations [24]. LEED was done on samples that were cleaved at $20K$, showing diffraction spots from the 3.9 \AA arsenic lattice, but also spots at lower diffraction angles, associated with larger real-space distances: the spots from the $\sqrt{2} \times \sqrt{2}$ and 2×1 (and 1×2) reconstructions. These fractional spots disappear upon heating to above $200K$, and do not return after cooling. LEED $I(V)$ measurements performed on the same crystals are also consistent with the cleavage scenario argued above [26].

Although most of the measurements presented in this thesis were done on samples that were cleaved at low temperatures, some samples were cleaved at room temperature prior to cooling in the STM. This allows the half-layer to melt immediately, usually resulting in disordered topographies like figures 18d and 18e. Patches of $\sqrt{2} \times \sqrt{2}$ reconstruction are also seen in these warm cleaves. Apparently, however, these patches lack the long-range coherence required to produce fractional LEED spots.

3.2.2 $\text{Fe}_{1+y}\text{Se}_{1-x}\text{Te}_x$

The structure of the (11) family is clearly of type 2, see figure 21. The selenium and tellurium atoms, being one group to the right of arsenic in the periodic table, will have a charge of -2 . The iron atoms, as before, have a charge of $+2$. The iron layer contains twice as many atoms as each of the selenium/tellurium layers, giving a structural repeat unit with charges -2 , $+4$, -2 , if the cleavage occurs between two selenium/tellurium planes. Therefore, we expect to see in STM topographies a square lattice with a lattice constant of about $a_{\text{Se-Se}} = 3.9 \text{ \AA}$, with few irregularities or steps, since the Se-Fe-Se sandwiches are tightly bound internally, with only the van der Waals force connecting them to the other layers.

In figure 22, we do indeed see a square lattice of the correct size. Apart from the lattice, we see large protrusions, seemingly randomly placed. In roughly a month of STM measurements, a total of about $0.07 \mu\text{m}^2$ spread over ten macroscopically separate locations on two different cleaves, no features were seen that deviated from this general picture; no steps or surface reconstructions of any kind.

The protrusions are roughly 10 \AA in size, and at the highest point, they extend about 1.2 \AA above the lattice at these setup conditions ($V_{\text{Bias}} = 30 \text{ mV}$, $I_{\text{set}} = 2 \text{ nA}$, chosen for sharp topography). A likely candidate for the origin of these protrusions is the excess iron y in the $\text{Fe}_{1+y}\text{Se}_{1-x}\text{Te}_x$ structure. This excess iron concentration was measured to be in the order of 1 to 2% by means of Electron Probe Micro-Analysis (EPMA) for our samples. Simply counting the protrusions, e.g. 10 in the $(100 \text{ \AA})^2$ area imaged in figure 22, over a sufficiently large area, we arrive at a concentration of 0.014 protrusions per $a_{\text{Se-Se}}^2$. Assuming the protrusions are indeed caused by excess iron atoms, this gives a

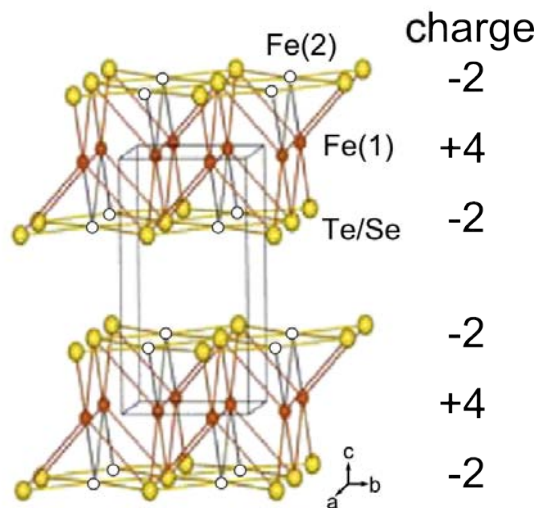


Figure 21: The structure of $\text{Fe}_{1+y}\text{Se}_{1-x}\text{Te}_x$. The y excess iron ends up in the usually empty Fe(2) positions, shown as white circles, in the Se/Te plane. Adapted from [27]

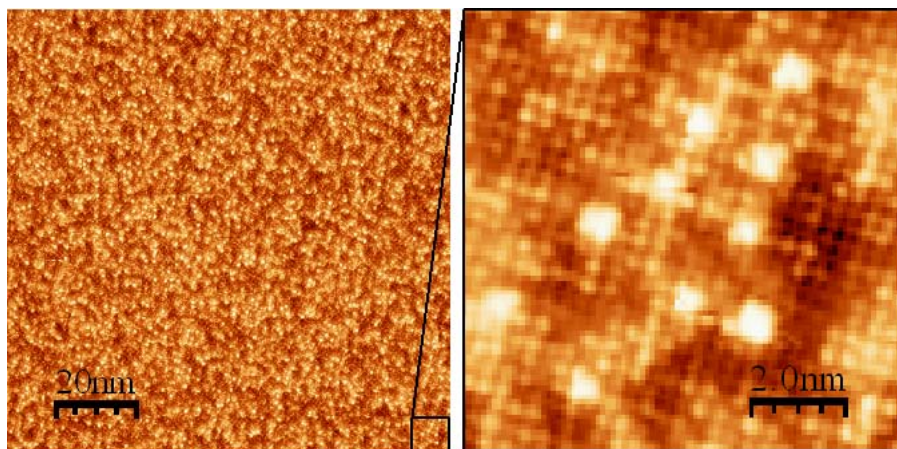


Figure 22: Typical topographic image of $\text{Fe}_{1+y}\text{Se}_{1-x}\text{Te}_x$. Set-up conditions for this image were $V_{Bias} = +30\text{mV}$, $I = 2\text{nA}$.

concentration of 1.4% excess iron: the iron layer has twice the number density of a single Se layer, but there are also twice as many Se layers as Fe layers in the crystal. This is in agreement with the less accurate EPMA measurement.

To dispel any doubts that the protrusions are indeed the excess Fe atoms, we can look at their locations with respect to the Se/Te lattice. The excess

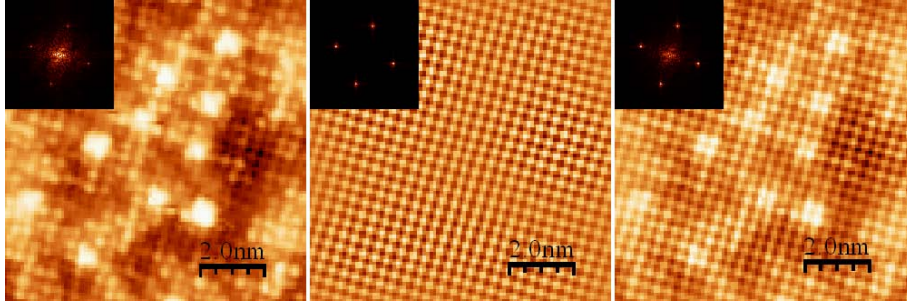


Figure 23: Fourier filtering a topographic image to determine the position of the protrusions relative to the lattice. (a) The raw topography and its Fourier transform. (b) The square lattice only, filtered out by removing everything in the Fourier transform except the atomic spots. (c) A combination of (a) and (b). The protrusions are now clearly identifiable as being located in the centres of squares of Se/Te atoms. Note: This is no longer an actual topography.

iron atoms end up in the Fe(2) position, which is in the selenium/tellurium plane, in the center of a square formed by 4 selenium/tellurium atoms. So, if the protrusions are the excess iron atoms, their centers should coincide with the centers of squares of Se/Te atoms.

The size of the protrusions makes it so they obscure the Se/Te atoms around them, making it difficult to see the position of their center with respect to the lattice. To image their position more clearly, we can enhance the visibility of the Se/Te lattice by Fourier filtering. We take the raw image (figure 23a) and Fourier transform it (inset). The Fourier transform consists of a center peak containing the large scale variations, and 4 sharp peaks in the 4 lattice directions, at $1/(3.9\text{\AA})$ from the center. We remove everything except these lattice spots, and transform back, leaving us with an image of only the lattice (figure 23b). In figure 23c, the raw data is overlaid with the lattice multiplied by 4 (in terms of apparent height, or signal strength in such a false color plot), i.e. it is $c = a + 4b$. This enhances the visibility of the atomic lattice, while still allowing us to see the protrusions as features that are much brighter than the surroundings.

In this enhanced image, we see that the protrusions have turned into squares of 4 bright atoms. This means the centers of the protrusions were in the center of these squares, as they should be if they are the excess iron atoms. If the protrusions were, for example, impurities that are substituted for a Se atom, the enhanced image would show them as fourfold symmetric features with a single brightest center atom. The entire area imaged in figure 22 shows the same features, when analysed in the same manner, as this smaller zoomed-in area. The inescapable conclusion is that the protrusions seen in our STM topographs of $\text{Fe}_{1+y}\text{Se}_{1-x}\text{Te}_x$ are the excess iron atoms.

3.3 Spectroscopy

The spectroscopy measurements in this thesis were focused on the superconducting gap of the pnictides. To get an idea of what is meant by the superconducting gap, it is instructive to look at the excitation spectrum of a simple superconductor, as predicted by BCS theory. Bardeen, Cooper and Schrieffer proposed for the superconducting condensate a ground state of the following form:

$$|\Psi_{BCS}\rangle = \prod_{\vec{k}} u_{\vec{k}} + v_{\vec{k}} c_{\vec{k}\uparrow}^\dagger c_{-\vec{k}\downarrow}^\dagger |0\rangle. \quad (8)$$

Here, $c_{\vec{k}\uparrow}^\dagger$ is a creation operator for an electron with momentum \vec{k} and spin up. The combination of the two creation operators $c_{\vec{k}\uparrow}^\dagger c_{-\vec{k}\downarrow}^\dagger$ thus creates out of the vacuum state $|0\rangle$ a pair of electrons with opposite spin and momentum: a Cooper pair. These Cooper pairs can exist, $v_{\vec{k}} = 1$, or not exist, $u_{\vec{k}} = 1$, or a superposition of the two, at every \vec{k} . Normalization requires $|u_{\vec{k}}|^2 + |v_{\vec{k}}|^2 = 1$. Calculating the minimum energy of this system gives

$$|E_{\vec{k}}|^2 = |\epsilon_{\vec{k}}|^2 + |\Delta|^2, \quad (9)$$

where $E_{\vec{k}}$ is the energy dependence on momentum for single electrons in the superconducting state, while $\epsilon_{\vec{k}}$ is the same in the normal state. The Δ is half of the binding energy of a Cooper pair. The density of states, which is what can be measured by STS, is then as follows:

$$g_{SC}(E) = \begin{cases} 0, & |E| < \Delta \\ \frac{|E|}{(E^2 - \Delta^2)^{\frac{1}{2}}}, & |E| \geq \Delta, \end{cases} \quad (10)$$

which is plotted in figure 24. In this simple BCS superconductor, the density of states is zero for energies that are closer to E_F than Δ . This density of states “piles up” in two coherence peaks, at $E = -\Delta$ and $E = +\Delta$, making the distance between them, the gap size, 2Δ . This general structure of the density of states, with a region of low or zero density of states in between two coherence peaks, is called the superconducting gap.

Scanning tunneling spectroscopy is uniquely suited to measuring these superconducting gaps. One main reason for this is its high energy resolution (in the order of 1 meV for our experiments, down to 0.1 meV for the world’s best, compared to e.g. ARPES which struggles to reach below 1 – 2 meV resolution). Another reason is the fact that both the occupied states below E_F and the unoccupied states above E_F can be probed, as opposed to ARPES which works by emission of electrons from the sample via the photoelectric effect, and can thus only probe the occupied states. To get a spectrum with two coherence peaks in ARPES, a symmetrization (which assumes particle-hole symmetry in the DOS) is required, around a Fermi level that must be determined separately by measuring on e.g. a gold surface.

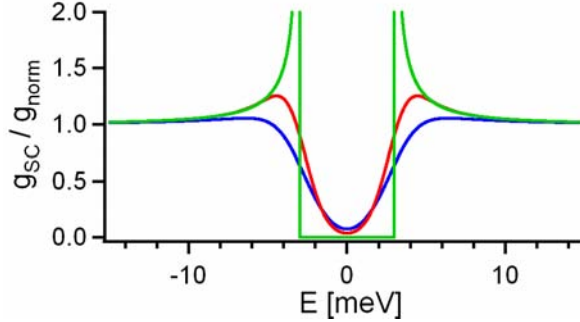


Figure 24: The density of states of a BCS superconductor (green) and two simulations of an STM measurement of it (red and blue). Values used: $\Delta = 3\text{meV}$, $T = 4.2\text{K}$, $\Gamma = 0.5\text{meV}$ (red), $\Gamma = 1\text{meV}$ (blue), broadened by a Gaussian of width 1meV to account for experimental resolution.

Of course, STS measurements are not perfect. Various effects can cause a broadening of the measured spectra. One is the fact that measurements are always done at finite temperature. This causes a broadening whose magnitude can be quickly estimated as $k_B T$, which is 0.4 meV at liquid helium temperatures. Another source of broadening is the lock-in amplifier. To get a dI/dV signal, it must add an alternating voltage with a certain amplitude to the bias voltage, which of course smears out the signal over a width equal to this amplitude.

Finally, when tunneling into superconductors, a relevant effect is the finite lifetime of quasiparticles [28]. A simplified way to account for this is to introduce an imaginary part to the energy in $g(E)$. The BCS density of states then becomes

$$g_{SC}(E, \Gamma) = \frac{|E - i\Gamma|}{((E - i\Gamma)^2 - \Delta^2)^{\frac{1}{2}}}. \quad (11)$$

The real part of this is then what is actually measured. An example of what we might actually expect to measure is plotted together with the ideal curve in figure 24. This is the density of states in (11) convoluted with a Fermi-Dirac distribution to simulate the effect of finite temperature, and then convoluted with a Gaussian to simulate the finite energy resolution caused by e.g. the lock-in amplifier.

3.3.1 Spectroscopy of underdoped $\text{Ba}(\text{Fe}_{1-x}\text{Co}_x)_2\text{As}_2$

In the research group hosting my MSc research project, STM/STS measurements had already been carried out on optimally doped $\text{Ba}(\text{Fe}_{1-x}\text{Co}_x)_2\text{As}_2$. As part of my research, I extended these measurements to the underdoped regime. The spectroscopic results of these investigations form the basis for this section.

The samples used for this study of underdoped $\text{Ba}(\text{Fe}_{1-x}\text{Co}_x)_2\text{As}_2$ had a cobalt content of $x = 0.035$ as measured by EPMA, and a superconducting T_c

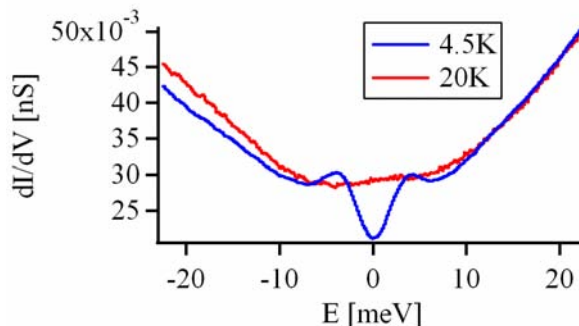


Figure 25: The superconducting gap of underdoped $\text{Ba}(\text{Fe}_{1-x}\text{Co}_x)_2\text{As}_2$. The gap is present in the spectrum at 4.5 K, but not at 20 K (above $T_c = 14$ K) . Lock-in modulation amplitude 0.4 mV.

of 14K measured by resistivity. Looking back at the phase diagram from [11] shown in figure 15, we see that these two facts do not seem to agree: a cobalt concentration of $x = 0.035$ would give a lower T_c , if this phase diagram is correct. A fellow MSc student, Rein Huisman, has generated a (T, x) phase diagram for $\text{Ba}(\text{Fe}_{1-x}\text{Co}_x)_2\text{As}_2$ from resistivity measurements on our own single crystals. Although the general form is similar to the phase diagram from [11], the fact that - for example - the T_c of the underdoped sample concerned is higher would suggest that our crystals are of even better quality than those discussed in [11]. In any case, we can be confident that the samples used are indeed underdoped, in the region where the spin-density wave state coexists with superconductivity in the same sample.

The tunneling density of states as a function of energy of this material, near the Fermi energy, is roughly V-shaped, with a minimum near E_F and rising linearly away from E_F up to at least $|E| = 150\text{meV}$.

In a high resolution spectrum over a more limited energy range, figure 25, we can easily discern the superconducting gap in the low temperature spectrum. The peak-to-peak energy separation for this particular spectrum is 7.5meV. There is some spatial variation, and the average peak-to-peak separation that we see is 8.2 meV, giving us an average value for Δ of 4.1 meV. We can compare this to the optimum doped case [29], where the modal peak-to-peak energy separation is 14meV, for a sample with a T_c of 22K. An important measure of the coupling behavior in a superconductor is the value of $2\Delta_{SC}/k_B T_c$. If we take the peak-to-peak distances to be $2\Delta_{SC}$, this gives us values of $2\Delta_{SC}/k_B T_c = 6.6$ in the underdoped case, and 7.4 in the optimum doped case. In both cases, this is well above the BCS weak-coupling limit of 3.52.

Point contact tunneling studies [30] on both K-doped ($\text{Ba}_{1-x}\text{K}_x\text{Fe}_2\text{As}_2$) and P-doped ($\text{BaFe}_2(\text{As}_{1-x}\text{P}_x)_2$) compounds, however, consistently give the result $2\Delta_{SC}/k_B T_c = 3.1$, at various doping concentrations. It seems that cobalt doping increases $2\Delta_{SC}/k_B T_c$, while doping on other sites does not, and that with

increasing cobalt doping $2\Delta_{SC}/k_B T_c$ also increases. This trend continues for overdoped samples [23]. A possible explanation for this is that cobalt doping has a secondary effect: it introduces scatterers (the Co atoms) in the Fe layer, where all the physics takes place. This could suppress T_c [31] while having less effect on the value of Δ_{SC} , thereby increasing $2\Delta_{SC}/k_B T_c$. Doping with K or P, which replace Ba and As atoms respectively instead of Fe, seemingly has less impact on the scattering felt by the Fe 3d electrons which are the charge carriers involved in forming the superconducting state.

Up to now, we have assumed that the gap-like structure in figure 25 is indeed an experimental measurement of the superconducting energy gap. In the cuprate superconductors, a similar gap-like structure was observed, which was however also present in the density of states when measurements were taken above T_c . This gap-like structure has since been termed a *pseudogap*[32]. It has also been predicted to exist in the pnictides [9]. To confirm that the gap-like shape that we see in our spectra is indeed the superconducting energy gap, it is essential to check whether the gap disappears when the sample is heated to above T_c . As can be seen from the red curve in figure 25, measured at the same position as the blue curve but at 20 Kelvin, the gap does indeed go away above T_c . This means that it is not a pseudogap.

The spectrum in figure 25 was taken on a $\sqrt{2} \times \sqrt{2}$ surface. The structure of the barium atoms on the surface could very well affect the spectrum. It turns out that on a 2×1 surface, the spectra are essentially the same as the one shown in figure 25. However, on disordered barium and on rods, the spectra can differ wildly. Often, on regular surfaces, the gap is less clear than in figure 25, with the coherence peaks present only as shoulders, similar to the blue curve in figure 24. This suggests that Γ might vary from location to location, which would explain the variation in spectra. Some tips also display clearer gaps than others. With a tip that shows a clear gap, the gap is present at any location on a sample. Knowing this, we can rule out the possibility of phase separation into distinct regions of superconductivity and SDW order: the coexistence of the two, which was one of the main motivations behind studying the underdoped compound, is in fact present on length scales below tens of nanometers.

Evidence from other techniques suggests that $\text{Ba}(\text{Fe}_{1-x}\text{Co}_x)_2\text{As}_2$ has two gaps, of different size. For example, experiments done in Stanford [34] on underdoped samples, measuring the penetration depth as a function of temperature, find that a model with two BCS-type gaps fits the $\lambda(T)$ curve much better than a single gap. They find for the two gap sizes $\Delta_1 = 2.6k_B T_c$ and $\Delta_2 = 0.8k_B T_c$, corresponding to $\Delta_1 = 3.1\text{meV}$ and $\Delta_2 = 1.0\text{meV}$ for our T_c of 14K . Optics experiments on our own optimally doped samples also see evidence for a double gap [33]. So we seem to be seeing the larger gap (we have $\Delta = 4.1\text{meV}$), and missing the smaller gap if it exists. This double gap scenario is reminiscent of the superconductor MgB_2 [35].

The density of states of a double BCS-type gap would, in the ideal case, look like a sum of two single gap densities of states. This is plotted in figure 26 (red curve), with the aforementioned $\Delta_1 = 3.1\text{meV}$ and $\Delta_2 = 1.0\text{meV}$. The relative intensities of the two were taken to be equal for simplicity. At first glance,

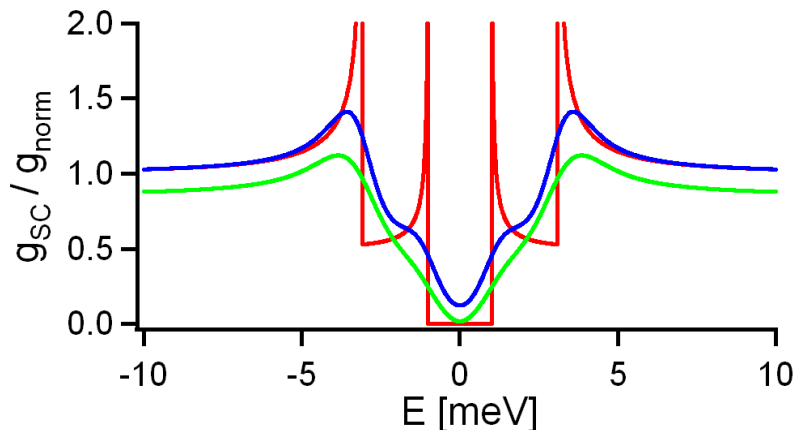


Figure 26: The double gap scenario. The red curve is the theoretical density of states for two BCS gaps, $\Delta_1 = 3.1\text{meV}$ and $\Delta_2 = 1.0\text{meV}$, with equal relative intensity. The blue curve accounts for temperature broadening at 4.2K , and the green curve (shifted down by 0.15 for clarity) further accounts for lifetime broadening with $\Gamma = 0.2\text{meV}$ and experimental resolution.

this should be easily distinguishable from a single gap density of states, but in a real measurement, at 4.2K , the smaller gap is almost completely washed out by the temperature broadening alone (blue curve). The coherence peaks have been reduced to shoulders on the slope of the larger gap. Accounting for lifetime broadening with an optimistically low $\Gamma = 0.2\text{meV}$ and experimental resolution with a 0.5meV wide Gaussian removes all but a hint of the smaller gap (green curve). From these measurements of underdoped $\text{Ba}(\text{Fe}_{1-x}\text{Co}_x)_2\text{As}_2$, we therefore cannot conclude that there is only a single gap, even though we only see one.

Knowing that there is a superconducting gap, an interesting thing to try to measure is the spatial variation of the gap size. This was done on a patch of $\sqrt{2}\times\sqrt{2}$ reconstruction, shown in figure 27a. On this piece of surface, 128 by 128 spectra were taken, with the aim of making a 128 by 128 pixel gap map. This was unsuccessful, as there was too much noise in the single spectra to reliably determine the gap value. By averaging squares of 4 by 4 spectra, however, a 32 by 32 pixel gap map was possible, shown in figure 27b. This was done in an automated way by fitting to the two peaks on either side of E_F . For some pixels, this fit failed, but the gap size could still be estimated by manually examining the spectrum. This manual estimation had to be done for about 5% of the pixels.

Figure 27c shows the distribution of gap sizes in this map. The average Δ is 4.1meV , with a standard deviation of 0.7meV .

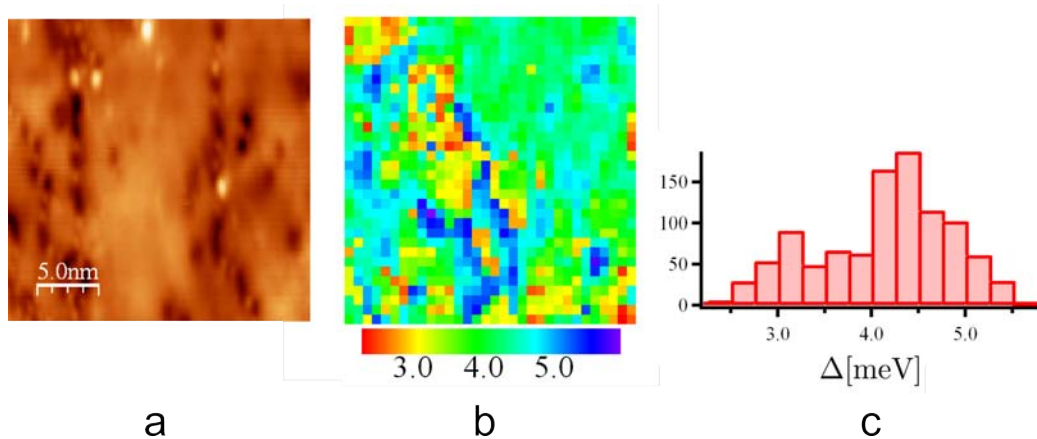


Figure 27: A gap map (b) on a $(240\text{\AA})^2$ patch of $\sqrt{2}x\sqrt{2}$ reconstruction (a). (c) The distribution of gap sizes.

3.3.2 Spectroscopy of $\text{Fe}_{1.014}\text{Se}_{0.45}\text{Te}_{0.55}$

Research on the iron pnictides at the WZI has focused mainly on the (122) systems, of which there is a large collection of nice single crystals of various dopings. During my project, crystals of the (11) family became available, and a short excursion was made to see what interesting spectroscopic results could be extracted from them.

The samples of $\text{Fe}_{1.014}\text{Se}_{0.45}\text{Te}_{0.55}$ used for these measurements were found to superconduct at $12.5K$. As in the $\text{Ba}(\text{Fe}_{1-x}\text{Co}_x)_2\text{As}_2$ case, we expect to see signs of this superconductivity around E_F , in the form of a gap. At first glance, however, we do not see a clear gap-like structure in spectra taken at $4.5K$ (see figure 28a). The spectrum is V-shaped, as is the case in $\text{Ba}(\text{Fe}_{1-x}\text{Co}_x)_2\text{As}_2$, but is missing the large coherence peaks that were so clearly visible in the (122) compound.

Looking more closely at the spectrum in figure 28a, and comparing it to the one taken at $15K$, we note that there are two shoulders, on either side of E_F , which are not present in the high-temperature spectrum. These might be remnants of the coherence peaks, greatly flattened for some reason. Indeed, when we divide the low-temperature spectrum by the high-temperature spectrum, the peaks are clear as day (figure 28b). If we take the peak-to-peak distance as 2Δ , we get a Δ of 4.5meV , and $2\Delta_{SC}/k_B T_c = 8.4$. Taking the peak-to-peak distance as the true value of 2Δ is rather optimistic, though: the gap is not very deep at all, with the difference between the top of the higher peak and the bottom of the gap being only 10% of the full density of states. This indicates that there was a lot of broadening, which pushes the top of the peak out from the center, as can be seen in figure 24.

In an optical conductivity/reflectivity experiment, Homes et al. [36] see evidence for 2 gaps, as in the barium compound. In their samples of $\text{FeSe}_{0.45}\text{Te}_{0.55}$

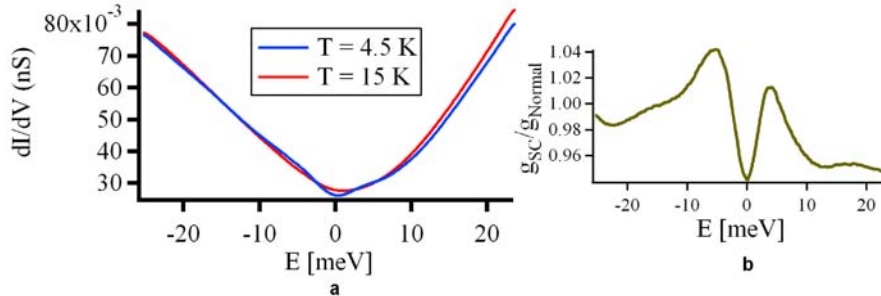


Figure 28: (a) Tunneling density of states of $\text{Fe}_{1.014}\text{Se}_{0.45}\text{Te}_{0.55}$ at 4.5K and at 15K, which is above $T_c = 12.5\text{K}$. Lock-in modulation amplitude: 0.8 mV. (b) The 4.5K spectrum divided by the 15K one, showing clearly the two coherence peaks, with peak to peak separation of $2\Delta = 9.0\text{meV}$.

(excess iron content not specified) with $T_c = 14\text{K}$, they see gaps of size $\Delta_1 = 2.5\text{meV}$ and $\Delta_2 = 5.1\text{meV}$, or $2\Delta_1/k_B T_c = 4.1$ and $2\Delta_2/k_B T_c = 8.5$. They note also that only 20% of the free carriers enter the superconducting condensate, providing a possible alternative explanation (besides large amounts of broadening) for why the gap we see is so shallow. Again, we see no evidence of the smaller gap.

Hanaguri et al. [37] do see a full gap, with a nearly zero density of states at E_F , of size $\Delta = 1.7\text{meV}$ ($2\Delta/k_B T_c = 2.7$). They see no hint of the larger gap, only a small asymmetric feature at $\pm 4\text{meV}$ for which they do not offer an explanation. They see these spectra at locations far (7nm) from the nearest excess iron atom, which is farther than is possible in our crystals due to our higher concentration of excess iron (1.4 % vs roughly 0.15% estimated from the topograph they show; they do not mention the composition of their samples at all). This difference in excess iron concentration could be an explanation for why our spectra have such a large residual conductance at E_F compared to theirs.

The shallowness of the gap in our measurements of $\text{Fe}_{1.014}\text{Se}_{0.45}\text{Te}_{0.55}$, which is even more pronounced than it is in the $\text{Ba}(\text{Fe}_{1-x}\text{Co}_x)_2\text{As}_2$ case, made it impractical to make a gap map: The gap is only discernible in averages of hundreds of spectra.

An attempt was made to find so-called quasiparticle scattering interference (QPI) patterns [38]. The idea is that when quasiparticle states \vec{k}_1 and \vec{k}_2 are mixed by some form of scattering, this causes an interference pattern with wave vector $\vec{q} = \vec{k}_1 - \vec{k}_2$ in the size of the quasiparticle wavefunction. This can be measured with STM as a modulation of the LDOS(E) with a period $\lambda = 2\pi/|\vec{q}|$. This allows the normally real-space probe STM to probe k -space or, in fact, q -space instead.

The flat regular surface of $\text{FeSe}_{1-x}\text{Te}_x$ makes it ideally suited to measuring QPI, but it is still quite an ambitious measurement. The heavy hitters of the

STM world that are publishing their QPI results use custom-built STMs costing many millions of euros, while our humble setup was commercially built and cost of order one tenth as much.

The results of our attempt at measuring QPI are shown in figure 29. On the area shown in figure 29a, 128 by 128 spectra were taken. As described in section 2.1, we can make cuts at a constant energy through this grid of spectra to get $\text{LDOS}(E, \vec{r})$. In figure 29b is plotted the ratio of $\text{LDOS}(+E, \vec{r})$ and $\text{LDOS}(-E, \vec{r})$, in this case for $E = 2\text{meV}$. This ratio should have an improved contrast of the QPI pattern over the LDOS itself [37]. The energy $E = 2\text{meV}$ turned out to show the most contrast.

At first glance, the LDOS ratio does not seem to show much of a regular pattern, so we turn to its Fourier transform, on the right. Standard procedure here is to do some data massaging on this Fourier transform: Low-pass filters, symmetrization, and subtracting a Gaussian to get rid of the center peak for example. However, even in the raw data a four-fold symmetric pattern is visible. There are two distinct distances and directions: The spot with a blue circle corresponds to a distance of 3.9 Å, and lies in the same direction as the Se/Te lattice. Although the fact that this is an LDOS picture and not a topography, and that we even divided out the $\text{LDOS}(-E)$, means that topographic information should be gone, it is still not terribly surprising to see a pattern of this size in this direction: It could simply come from the atomic lattice. The spots with a red circle, however, correspond to a distance of 5.6 Å and are rotated by 45 degrees compared to the blue spots.

Comparing with Hanaguri et al.[37], the blue spots are what they call \vec{q}_3 , and in k-space represent a scattering from an electron pocket at M to an electron pocket at a different M point. The red spots are what they call \vec{q}_2 , and in k-space represent a scattering from a hole pocket at Γ to an electron pocket at M . They do not mention explicitly that \vec{q}_3 coincides with a lattice vector. The tacit assumption is made that taking the ratio of the two LDOS value at positive and negative bias will remove any effect of the atomic lattice, and that the fact that the spots are still visible after the division means that their origin is indeed quasiparticle interference. They do see intensity variations in the peaks as a function of magnetic field, supporting their argument, but it still seems quite a bold assumption to say that the lattice is not simple the origin of these spots.

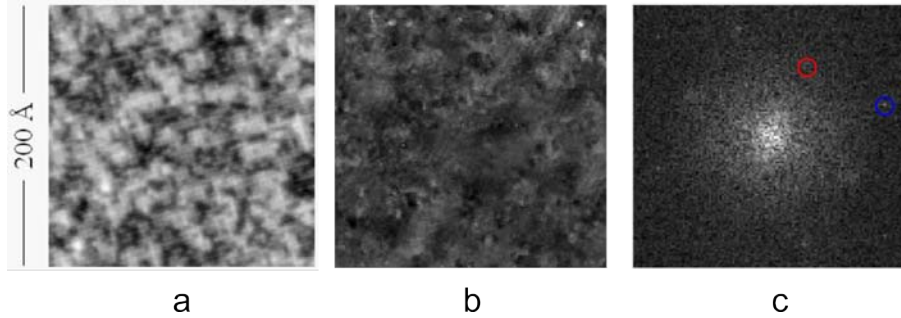


Figure 29: (a) The topography on which this QPI measurement was done. (b) The LDOS ratio at $E = 2\text{meV}$. (c) The Fourier transform of (b). The QPI pattern is fourfold symmetric, with 2 distinct peaks, marked with a blue and a red circle.

4 Conclusion

Scanning tunneling microscopy is a powerful technique that can be used to draw many conclusions about the pnictide superconductors.

Conclusions from topographical information

The cleavage surface of the (122) family was confirmed to be the e.g. barium layer, half of which remains on either side of the cleavage plane. Steps were very rare. In the barium compound, various surface reconstructions were observed for this half-layer, and a model was given which explains all of these in terms of the possible arrangements of atoms in the half-layer. Despite some lingering doubts among some in the surface science community, namely that the cleavage surface might be the arsenic layer, we can state with complete confidence that it is indeed the barium layer, in agreement with theoretical prediction. Further experiments might look at the surface of other members of the (122) family, to see if e.g. calcium or europium atoms arrange in the same way as the barium atoms do. Accurate determination of the surface structure is essential, as there are already numerous ARPES investigations that have been done on the (122) compounds.

In the (11) family, there is no doubt as to the cleavage surface: It is a 3.9 \AA square lattice, which must be the selenium/tellurium layer. High tunneling current features on this surface, leading to protrusions in the apparent height, were found to coincide with the so-called Fe(2) position, confirming them to be the excess y iron atoms present in $\text{Fe}_{1+y}\text{Se}_{1-x}\text{Te}_x$. They also occurred with a number density that was in agreement with EPMA measurements of the iron concentration. Using the fact that these protrusions are the excess iron atoms, it was possible by counting them to determine the composition of our sample more accurately than the original EPMA measurements.

Conclusions from spectroscopy measurements

Spectroscopy measurements revealed that our samples of $\text{Ba}(\text{Fe}_{1-x}\text{Co}_x)_2\text{As}_2$ with $x = 0.035$ (underdoped, $T_c = 14\text{K}$) displayed a single superconducting gap of average size $\Delta = 4.1\text{meV}$, or $2\Delta/k_B T_c = 6.6$. The possible presence of another, much smaller gap could not be ruled out due to resolution limitations. This superconducting gap disappeared when measuring at the same location at a temperature above T_c , confirming that it is indeed the SC gap and not a pseudogap of some sort. This superconducting gap is present at all locations on a sample, indicating a lack of phase separation into distinct areas of SDW and of SC state; the coexistence of the two is present at a microscopic level.

Further studies could focus on other doping concentrations, different types of doping such as hole doping with potassium replacing barium, and different compounds within the (122) family such as the europium or the calcium compound.

Spectroscopy on $\text{Fe}_{1.014}\text{Se}_{0.45}\text{Te}_{0.55}$ with a T_c of 14K revealed a gap of size $2\Delta = 9\text{meV}$, or $2\Delta/k_B T_c = 8.4$. An attempt at a QPI measurement was a moderate success, showing that it is possible even with our commercially available STM setup. Further studies of the (11) family would likely benefit from samples with a lower concentration of excess iron.

The (111) family could also be studied: it is likely to have a nice flat cleavage surface, suitable for STM and other surface sensitive techniques. The reason that it has not been studied extensively seems to be that it is rather hard to grow single crystals of it. Finally, the (1111) family is probably unsuitable for surface studies: following the same arguments as were made for the (122) family, its surface would have to be heavily reconstructed, since an LaO trilayer with the same structure as the universal FeAs trilayer is not nearly as easily split in two as a collection of barium atoms. Still, it could be interesting to have a look at the surface in STM, to see if it is indeed as much of a mess as expected.

Acknowledgements

After having been part of a research group for more than a year, there are many people to thank for their contributions. First off, I would like to thank my supervisor, Mark Golden, for the enthusiasm with which he guides the research done in the group. Freek Masee, the PhD student who worked on the STM alone until I started my project, taught me everything there is to know about the Createc LT-STM and all of the experimental necessities that go with it, and guided me in the lab until I was skilled enough to perform the experiments alone: I couldn't have done it without his tireless guidance. Freek's PhD supervisor, Jeroen Goedkoop, is responsible for the fact that we have such a nicely working STM in the first place; thanks go to him as well.

Yingkai Huang is the crystal growth expert who grows our excellent pnictide single crystals. I thank Huib Luigjes and fellow MSc student Rein Huisman for their resistivity measurements on these crystals, an essential first step in figuring out what's going on inside. Huib also provided expert technical support for the STM.

Then of course, there is the rest of the QEM group at the WZI. Anne de Visser, whose more outside-in view of the pnictide superconductors offers valuable insights (he has his own research group, currently focused on the ferromagnetic superconductors), Erik van Heumen, a postdoctoral researcher who works on the pnictides as well, Erik Slooten, the freshest PhD student in the group, Sanne de Jong, ARPES expert who finished his PhD during my time in the group and moved on to a postdoc position at Stanford, fellow MSc student Jesse Klei who did LEED $I(V)$ experiments on the pnictides, and finally veteran researcher Jacques Klaasse, who went to enjoy his retirement during my time in the group. They all are instrumental in providing a pleasant atmosphere that is conducive to research.

On the more technical side of things, I would like to thank Hugo Schlatter for his help with both the gold test sample and the thermometer sample, and Hans Agema for his insights in reducing electronic noise.

Finally, I would like to thank the funding agency Stichting FOM.

Publication List

Research done during this MSc project resulted in the following publications:

- “Cleavage surfaces of the $\text{BaFe}_{2-x}\text{Co}_x\text{As}_2$ and $\text{Fe}_y\text{Se}_{1-x}\text{Te}_x$ superconductors: A combined STM plus LEED study”, F. Masee, S. de Jong, Y. Huang, J. Kaas, E. van Heumen, J. B. Goedkoop, and M. S. Golden, Phys. Rev. B 80, 140507(R) (2009)
- “Momentum dependent electron and hole dynamics and electron-phonon coupling in iron pnictides from time- and angle-resolved photoemission spectroscopy”, S. Thirupathaiah, E.D.L. Rienks, H.S. Jeevan, R. Ovsyanikov, E. Slooten, J. Kaas, E. van Heumen, S. de Jong, H.A. Duerr, K. Siemensmeyer, R. Follath, P. Gegenwart, M.S. Golden, J. Fink. Preprint: arXiv:1007.5205v1.

References

- [1] Y. Kamihara et al., J. Am. Chem. Soc. 2008, 130, 3296-3297
- [2] Kyle McElroy, Scanning Tunneling Microscopy Studies in both Real- and Momentum-space of the Doping Dependence of Cuprate Electronic Structure (PhD Thesis, UC Berkeley, 2005)
http://people.ccmr.cornell.edu/~jcdavis/theses/Thesis_KyleMcElroy.pdf
- [3] J. Bardeen, Phys. Rev. Lett. 6, 57 (1961)
- [4] J. Tersoff, D. Hamann, Phys. Rev. B 31, 805 (1985)
- [5] Milan P. Allan, The Electronic Structure of the Nematic Materials $\text{Sr}_3\text{Ru}_2\text{O}_7$ and $\text{Ca}(\text{Co}_x\text{Fe}_{1-x})_2\text{As}_2$, (PhD Thesis, University of St. Andrews, 2010)
- [6] S. Rousset et al., J. Phys.: Condens. Matter 15 (2003) S3363S3392
- [7] J.G. Ziegler, N.B. Nichols, Transactions of the A.S.M.E, v64 (1942), pp. 759-768
- [8] S. de Jong et al., Phys. Rev. B 79, 115125 (2009)
- [9] K. Ishida, Y Nakai, H. Hosono, J. Phys. Soc. Jpn., Vol. 78, No. 6, 062001
- [10] D. C. Johnston, arXiv:1005.4392v1, to be published in Advances in Physics (2010)
- [11] S. Nandi et al., Phys. Rev. Lett. 104, 057006 (2010)
- [12] M. Rotter et al., Phys. Rev. Lett. 101, 107006 (2008)
- [13] S. Jiang et al., J. Phys.: Condens. Matter 21 (2009) 382203
- [14] P. Alireza et al., J. Phys.: Condens. Matter 21 (2009) 012208
- [15] I. Mazin et al., Phys. Rev. Lett. 101, 057003 (2008)
- [16] M. Berciu et al., Phys. Rev. B 79, 214507 (2009)
- [17] V.I. Anisimov et al., Physica C 469, 442 (2009)
- [18] S. L. Skornyakov et al., Phys Rev B 80, 092501 (2009)
- [19] J. Zhang., Phys. Rev. B 79, 220502 (2009)
- [20] P.W. Tasker, J. Phys. C, Solid State Phys., Vol 12, 4977 (1979)
- [21] V.B. Nascimento et al., Phys. Rev. Lett. 103, 076104 (2009)
- [22] F.C. Niestemski et al., arXiv:0906.2761v1 (2009)
- [23] Private communication, Freek Massee

- [24] F. Massee et al., Phys. Rev. B 80, 140507 (2009)
- [25] M. Gao et al., Phys. Rev. B 81, 193409 (2009)
- [26] J. Klei, Low-Energy-Electron-Diffraction on Pnictide Superconductors (MSc thesis, Univ. of Amsterdam, 2010)
- [27] J. Lynn, P. Dai, Physica C 469 469476 (2009)
- [28] R.C. Dynes et al., Phys. Rev. Lett. 41, 1509 (1978)
- [29] F. Massee et al., Phys. Rev. B 79, 220517 (2009)
- [30] X. Zhang et al., Phys. Rev. B 82, 020515 (2010)
- [31] Y. Bang et al., Phys. Rev. B 79, 054529 (2009)
- [32] M.C. Boyer et al., Nature Physics 3, 802 - 806 (2007)
- [33] E. van Heumen et al., EuroPhys. Lett. 90, 37005 (2010)
- [34] L. Luan et al., Phys. Rev. B 81, 100501 (2010)
- [35] S. Tsuda et al., Physica B 312313 (2002) 150151
- [36] C. C. Homes et al., Phys. Rev. B 81, 180508 (2010)
- [37] T. Hanaguri et al., Science 328, 474 (2010)
- [38] J.E. Hoffman et al., Science 297, 1148 (2002)

A Appendix: Beamtimes at BESSY

Besides doing STM measurements at the van der Waals-Zeeman Institute in Amsterdam, during my MSc research project I also participated in ARPES experiments for a total of three weeks at the BESSY II synchrotron at the Helmholtz center in Berlin. These experiments were done using both the “1-cubed” and the “1-squared” ARPES end stations.

In a synchrotron, electrons are accelerated around a ring (240 meter circumference, in the case of BESSY II). Electromagnetic radiation is produced from these moving electrons by sending them through undulators. This produces photons of a very specific, controllable energy, with a high intensity, which makes them very well suited to doing ARPES experiments.

The 1-cubed end station is named for its intended energy resolution and measurement temperature: incident photons with an energy resolution below 1 meV, an electron analyzer with resolution below 1 meV, and a sample temperature less than 1 Kelvin. The 1-squared end station is intended to have the same energy resolution, but does not have the helium-3 cryostat that allows the 1-cubed to reach 1 Kelvin: it is only cooled by liquid helium-4. Not having the helium-3 cryostat does have a mitigating advantage in that the positioning of the sample is much less restricted.

Synchrotron time is a scarce resource, and many different research groups use the end stations over the course of a year, so the time is divided up into beamtimes: 1 to 2 week periods, during which you want to take as much data as possible, so you work day and night. This requires a team of people, and I functioned as the junior member of 2 such teams: one composed of members of our own research group at the WZI, and one a collaboration with a group at the Helmholtz center.

Despite the fact that the physical principle behind the technique is completely different, most of the actual activities when doing ARPES are rather similar to doing STM: samples need to be glued onto holders, introduced into the UHV through the load lock, cleaved, and transferred into the measuring position, cryostats need to be filled from dewars, and if all goes well, most of the time is spent behind a computer taking data. Doing this for 12-hour+ shifts often in the middle of the night adds an extra dimension, of course.

Data from these beamtimes was part of research to be published as “Momentum dependent electron and hole dynamics and electron-phonon coupling in iron pnictides from time- and angle-resolved photoemission spectroscopy”, S. Thirupathiah, E.D.L. Rienks, H.S. Jeevan, R. Ovsyannikov, E. Slooten, J. Kaas, E. van Heumen, S. de Jong, H.A. Duerr, K. Siemensmeyer, R. Follath, P. Gegenwart, M.S. Golden, J. Fink. Preprint: arXiv:1007.5205v1.

This introduction to a technique that gives k-space information about the electrons in a material, as opposed to the real-space information that STM provides, was quite interesting and enlightening.